Understanding heterogeneous and anisotropic porous media based on geometric properties derived from three-dimensional images

Rongrong Tian[1,3], Tingchang Yin[1,3], Yanmei Tian[1,3], Chen Yu[4], Jiazuo Zhou[5], Xiangbo Gao[1,3], Xingyu Zhang[3], Sergio Andres Galindo-Torres[2,3,6], and Liang Lei[2,3,6*]

[1]College of Environmental and Resources Science, Zhejiang University, Hangzhou, Zhejiang 310058, China

[2]Research Center for Industries of the Future, Westlake University, Hangzhou, Zhejiang 310030, China

[3]Key Laboratory of Coastal Environment and Resources of Zhejiang Province, School of Engineering, Westlake University, Hangzhou, Zhejiang 310030, China

[4]School of Chemistry and Materials Science, Hangzhou Institute for Advanced Study, University of Chinese Academy of Sciences, Hangzhou, Zhejiang 310030, China

[5]State Key Laboratory of Geomechanics and Geotechnical Engineering, Institute of Rock and Soil Mechanics, Chinese Academy of Sciences, Wuhan, Hubei 430000, China

[6]Institute of Advanced Technology, Westlake Institute for Advanced Study, Hangzhou, Zhejiang 310024, China

Corresponding author: Liang Lei (leiliang@westlake.edu.cn)

Key Points:

- A novel method for visualizing heterogeneity and anisotropy of porous media is proposed by deriving geometric properties from 3D images
- Stereographic projection is refined to statistically demonstrate heterogeneity and anisotropy in one plot
- The enhanced understanding of heterogeneity and anisotropy leads to a new approach to simplify geometric models in numerical simulation

Abstract

Natural porous media is generally heterogeneous and anisotropic. The structure of porous media plays a vital role and is often the source of the heterogeneity and anisotropy. In physical processes such as fluid flow in porous media, a small number of major features, here referred to as wide channels, are responsible for the majority of the flow. The thickness and orientation of these channels often determine the permeability characteristics. Typically, the identification of such major features is conducted through time-consuming and expensive simulations. Here we propose a prompt approach based on geometric properties derived from three-dimensional (3D) images. The size or radius of the major features is obtained via distance maps, and their orientations are determined by Principal Component Analysis. Subsequently, we visualize these features with color and color brightness according to their orientation and size, together with their location and distribution in 3D space. The simultaneous visualization of anisotropy (orientation) and heterogeneity (size) in one plot provides a straightforward way to enhance our understanding of pore structure characteristics. Besides, we propose a refined stereographic projection method to statistically illustrate both heterogeneity and anisotropy. Based on these insights, we further present a new way to compress the model size in numerical simulation, therefore significantly reducing the computational cost, while retaining its essential characteristics.

Plain Language Summary

Natural porous media, like soil or rock, have uneven structures which make it behave distinctively depending on their specific location or orientation. While this understanding has been widely acknowledged, conventional approaches rely on time-consuming and expensive methods such as field investigations, lab experiments, or numerical simulations to guess. Although imaging techniques such as X-ray computer tomography (CT) could provide the three-dimensional structure, there has yet to be no visualization technique that directly depicts the heterogeneity and anisotropy. Here, we propose a novel method that leverages feature size (heterogeneity) and orientation (anisotropy)to enable the simultaneous visualization of both size and orientation of targeted objects. A refined stereographic projection is introduced to statistically demonstrate the heterogeneity and anisotropy within one plot. To illustrate the effectiveness of our method, we utilize examples of coral pore structure, rock fractures, and ice crystals. The derived geometric features demonstrate a strong correlation with numerical simulation results of fluid flow, thereby proving its credibility and value in enhancing our comprehension of the heterogeneity and anisotropy of porous media. Based on these findings, we further propose a new approach to simplify geometric models in numerical simulations, which significatly reduces the computational cost while preserving the overall behavior.

1. Introduction

Heterogeneity and anisotropy are inherent features in natural porous media. These two features are the source of the unpredictable nature of sediments or geomaterials, as the structure along with the composition determines physical behaviors. Therefore, understanding the heterogeneity and anisotropy of porous media is critical to explain observed behaviors and predict outcomes in engineering practices.

The approach to consider the porous media with representative elementary volume (REV) is common. REV is based on the self-similarity of microstructures and can produce representative results when pore structure properties are stationary with increasing scale (Puyguiraud et al., 2020). Such an approach allows anisotropy but assumes that the media itself is homogeneous at a certain scale (Hunt & Sahimi, 2017; Bang & Lukkassen, 1999). It is ineffective for some porous media, like bio-generated structures. For instance, the coral pore structure shows some self-similarity and fractal behavior, the branches are scaled replicas of the whole structure (Martin-Garin et al., 2007). Since the branches are orientated differently, there is no scale that yields a representative volume for fluid flow. In other words, the heterogeneity and anisotropy are throughout the entire pore structure, and the concept of REV does not apply. Therefore, the attempt to simplify the actual pore structure must be based on the actual geometry.

Heterogeneity is critical in determining most physical properties of the porous media. Taking fluid flow in porous media as an example, seepages in porous media are often controlled by preferential flow channels (Hyman, 2020; Shigorina et al., 2021). Predicting these channels in porous media is vital in many geophysical scientific and engineering applications, such as oil and gas recovery (Chong et al., 2017; Chen et al., 2021), CO_2 geological storage (Xu et al., 2020; Shahriar & Khanal, 2023; Yang et al., 2018), and the estimation of subsurface contamination migration

(Sebben & Werner, 2016; Johnson et al., 2003). However, due to its heterogeneous porosity network, it is not practical to directly identify preferential flow channels.

It is difficult to properly consider heterogeneity without a real three-dimensional (3D) structure. The application of computer tomography (CT) technology (Flannery et al., 1987) and magnetic resonance imaging (MRI) (Budinger & Lauterbur., 1984) makes it possible to obtain the actual 3D pore structure, and its combination with digital image technology (Wildenschild & Sheppard, 2012; Lyu et al., 2021) enables the numerical representation of the porous media heterogeneity. However, two significant limitations remain for numerical simulations: high cost and a trade-off between the image resolution and sample volume (Silin & Patzek, 2006). The rebuilt model needs to be substantial enough to yield a meaningful result and have sufficient details to accurately depict fine pores (Jiang et al., 2013).

Image processing has contributed to numerical model simplification. For example, the connectivity of the pore structure can be identified by skeletonization (Ferreira & Nick, 2023, Lee et al., 1994), and thickness can be estimated by medial axis transform algorithms (Van der Walt et al., 2014) and distance transform algorithms (Grevera, 2007). On this basis, pore-network model, which was initially developed as regular lattices (Fatt, 1956), can be established to represent the connectivity and spatial arrangement of a 3D structure (Mahabadi et al., 2018; Jing et al., 2020). A pore-network model typically consists of pore nodes representing locally widest parts of pore space and bonds (sometimes called “pore throats”) connecting pores and the remainder (Jiang et al., 2017), and the flow calculation is much less expensive (Bultreys et al., 2016). However, the topology and geometry of the pore space are missing in modeling (Zhang et al., 2022), which may lead to significantly different flow properties (Nemati et al., 2020). In addition, the fractal theory is employed to characterize the pore irregularity (Zhang et al., 2020, Qin et al., 2023), yet the accuracy of this method remains uncertain since the spatial variation of pore size and pore network connectivity are neglected (Song et al., 2020).

125 The abovementioned efforts focus on heterogeneity, and the physical property in
126 an isotropic but heterogeneous media within a small area can be represented by a
127 scaler value. Anisotropy, on the other hand, requires the physical property to be
128 represented by a tensor rather than a scaler (Galindo-Torres et al., 2012; Ren &
129 Santamarina, 2018), which makes the problem more complicated. In geology,
130 researchers focus on analyzing the distribution of fracture orientations, the fraction of
131 void space, fracture local apertures, and preferred crystallographic orientation of
132 minerals. These factors lead to the anisotropy. The rose diagram (Degu & Hossain,
133 2012; Nemec et al., 1988) in geology are a common tool to describe the orientation
134 distribution, where the petal runs along the same direction as the object, and the
135 length of the petal depends on the frequency of the object in that direction. This
136 method typically plots the dip azimuth and dip angle separately, although these two
137 angles are actually coupled. Stereographic projection could be realized by projecting
138 the geometric elements of the 3D space onto the plane (Howarth, 1996), both the
139 longitude and latitude directions are plotted together. However, these approaches are
140 limited to a 2D view, in which the dependencies between the individual characteristics
141 cannot be investigated and the potential spatial regularities cannot be derived. Both
142 rose diagrams and stereographic projections are statistical methods, showing the
143 probability, but not the actual distribution in the space.

144 Overall, heterogeneity and anisotropy remain conceptual and can therefore be
145 obscure, without direct and vivid visualization. Frequently, they are considered
146 separately. Current literatures simplify the morphology of actual 3D structures when
147 considering heterogeneity and anisotropy due to limitations in computational
148 efficiency. Visualization, as a tool, has been demonstrated powerful for other purposes;
149 for example, visualizing pore size distribution using a 3D size map (Hilderand &
150 Ruegsegger, 1997) is a common practice (Ihli et al., 2017), and Grau et al. (2010)
151 described a method to visually identify the shortest path between two pores by
152 correlating the distance between a specific pore and its neighboring pores with color.

153 Therefore, it is promising and necessary to develop new visualization ways to
154 facilitate our understanding of the heterogeneity and anisotropy of porous media.

155 Here, we propose a method to simultaneously depict heterogeneity and
156 anisotropy in 3D structures while retaining their original morphology. We first show
157 how size-dependent heterogeneity and orientation-dependent anisotropy can be
158 derived from CT images. Then coral samples, rock fracture networks, and ice crystals
159 are selected as representative examples to present the visualization results. Based on
160 these results, we introduce a new approach to simplify geometric models in numerical
161 simulations.

162 2. Methods for Heterogeneity Characterization

163 A coral structure and its CT images are used to demonstrate our method (Figure
164 1). The axial canal, the lumen in the calyx, and the gastrovascular canal system
165 linking the axial canal and the lumen in the calyx constitute the main components of
166 the coral pore structure. Previous research (Li et al., 2021) indicates that the main
167 branchlets of the coral canal system are significant for understanding coral growth
168 patterns. The following workflow shows how the heterogeneous main branchlets are
169 extracted. This workflow can be summarized as follows: image segmentation, pore
170 structure isolation, 3D size measurement, and characterization and visualization of
171 size-dependent heterogeneity.

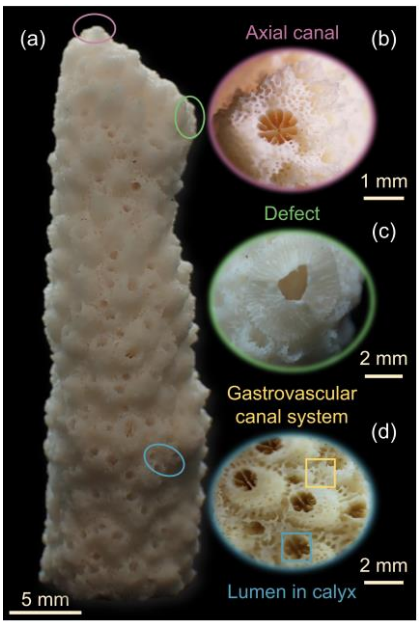

Figure 1. Details of a coral sample. (a) Holistic coral view. (b) Top pore corresponding to axis canal. (c) A defect in the sample. (d) Side pores corresponding to the lumen in the calyx and gastrovascular canal system.

2.1. Image Segmentation

An example image is shown in Figure 2a with a resolution of 12.8×12.8×12.8 μm per voxel. In this image, the void space and coral skeleton exhibit different voxel intensities, which quantifies the attenuations of X-rays as they pass through the corresponding points with different densities and atomic numbers. Image segmentation was carried out with ilastik (Berg et al., 2019). This machine learning-based tool offers significant advantages over traditional threshold segmentation and watershed segmentation methods. It learns from user-defined labels and then assigns image voxels to different groups in a batch-processing mode. The resulting image in Figure 2b contains two pixel values, 1 and 2, corresponding to 'coral skeleton' (black) and 'remainder' (white, including air and coral pores).

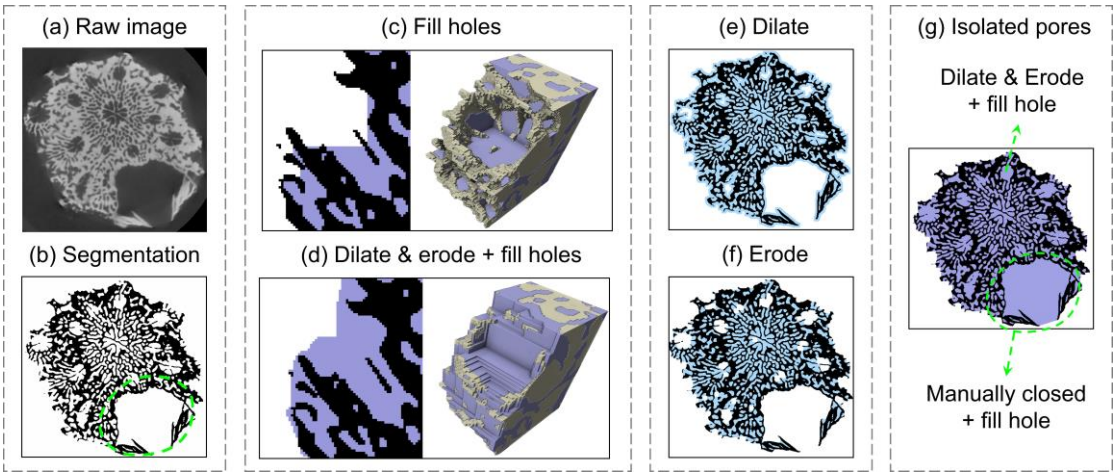

Figure 2. Isolation of coral pore structure. (a) Raw CT image of the coral sample. (b) Image segmentation. There is a notable defect circled in blue within the coral structure. (c) Inner pore isolation by 'fill holes' function. (d) Inner pore isolation by '3D dilate and erode' and 'fill holes' functions. The black phase represents the coral skeleton and is depicted as yellow in 3D structure, while the purple phase represents the inner pores. (e) Volume expansion by 'dilation'. (f) Volume shrinkage after 'erosion'. (g) Coral skeleton and the isolated coral inner pore structure.

2.2. Pore Structure Isolation

As seen in Figure 2b, the segmentation process separated the coral skeleton and the air-filled space, which can be further distinguished into inner pores and the space surrounding the coral skeleton. The coral pores are connected to the outside space and filled with the same substrate, air. It is therefore difficult to isolate the pore structure, and the challenge is to mathematically define the boundary between the pores at the coral edge and the outside space. Here, we propose two methods based on binary images of the coral skeleton.

The first method is to use the 'fill holes' function in ImageJ (Schindelin et al., 2012). In most cases, the inner pores are enclosed by the coral skeleton in 2D slices, allowing them to be filled with this function. The only issue occurs at the boundary between pores and the outside space, where a large space cannot be filled as they may appear to be open in 2D slices. One can apply the 'fill holes' function in the resliced

results in all x, y, and z directions. Performing boolean operations by subtracting the skeleton from the results after filling holes yields the coral pore structure. The visualization of the outcome is shown in Figure 2c.

In the second method, we apply the 3D ‘dilate’ function N times to close the pore openings (Figure 2e), and then apply the 3D ‘erode’ function the same N times to retreat from the over-occupied voxels while retaining the closed pore openings (Figure 2f). The value of N depends on the size of the pore openings: a small N value can not close large pores, whereas a large N value will render a more spherical coral outline, resulting in the loss of distinctive pore features. One can choose a good N value (N=5, in this paper) if the coral pore openings are relatively homogeneous in size. In the case of Figure 2a, which features a defect in the coral that requires a large N value that hurts the coral outline, we use a small N value to close small pore openings and manually close the large opening at the defect. Large pores or certain portion of the large pores could be left empty after N times of erosion-expansion cycles (Figure 2f). The unfilled portions are then filled with the 3D ‘fill holes’ function to obtain a summation of the coral skeleton and inner pores (Figure 2g). Then the subtraction of the coral skeleton from the summation yields the coral pore structure. Eventually, the three phases in the CT image: coral skeleton, pore structure, and air (outside space) are successfully distinguished in Figure 2g. The visualization of the result is shown in Figure 2d.

In general, the pore structure obtained by the first method is conservative, and some of the pore space is left as outer space. The second method aligns more closely with human judgment, although it typically introduces some additional voxels at the coral surface and sometimes requires manual intervention.

2.3. Feature size determination

The heterogeneity of porous media is primarily determined by morphology, which can be characterized by the local size of the 3D pore structure (Hilderand & Ruegsegger, 1997). Part of the three-phase image (Figure 3a) is used as an example to

illustrate the determination process of feature size, which includes 3D Euclidean distance (Merchant et al., 2023) measurement (Figure 3b) and 3D size determination (Figure 3c). Matrix A_1(a) in Figure 3a stores the initial voxel values of the three-phase images (Figure 2g). The algorithm of 3D distance and size measurement is accelerated in parallel (Chandra et al., 2001), and further details are given in Text S1-S5 in Supporting Information. Eventually, each voxel within a specific pore is assigned a value according to its corresponding 3D distance and size. Specifically, the voxel values in Figure 3b are assigned as the distance from the voxel to the closest pore wall, while the voxel values in Figure 3c are assigned as the radius of the largest inscribed circle that contains the voxel. These values are stored in the computed matrices A_2(a) and A_3(a), respectively.

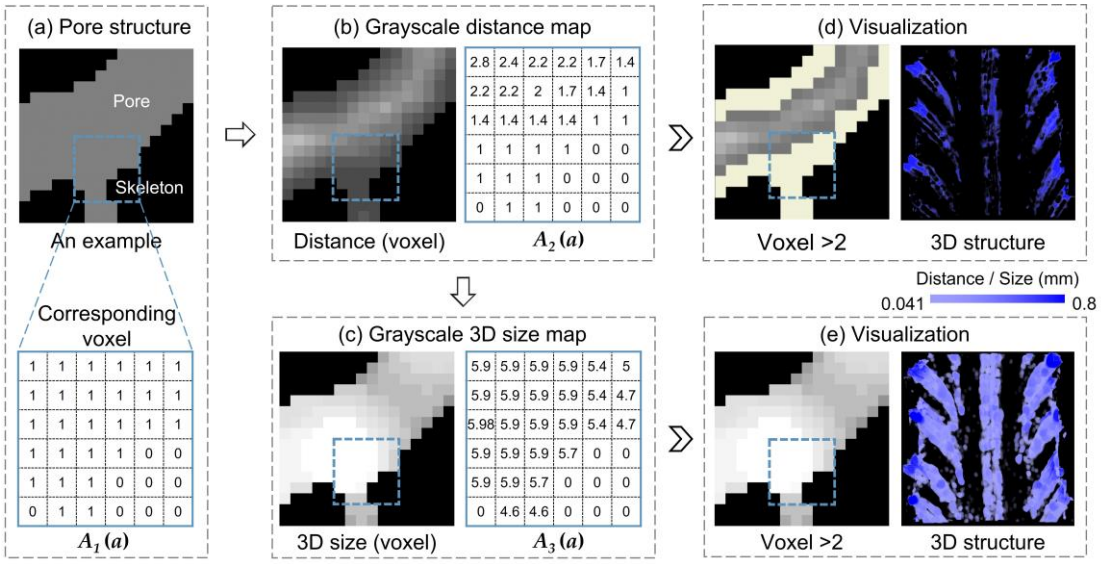

Figure 3. Coral pore size determination and visualization. (a) Isolated pore structure. (b, c) Grayscale 3D distance and size map. (d, e) Extraction of main pore networks after setting thresholds on the 3D distance and size maps, respectively. The same color bar is applied.

2.4. Heterogeneity Characterization and Visualization

The heterogeneity characterization should be combined with geophysics. For example, in fluid flow through a cylindrical tube, the average pore fluid velocity is

proportional to the square of the pore radius (R, similar to the value determined in the 3D size map) according to the Hagen-Poiseuille equation, and the overall flux is proportional to the fourth power of R. If the goal is to analyze the stiffness of the coral skeleton, then section modulus is proportional to the cube of the local skeleton diameter. In all these cases, the diameter or the feature size is the key.

For extracting main flow channels, we can set a threshold value to display only larger pores. If this operation is conducted on the 3D distance map, the pore surface voxels are all with the same value which indicates the distance to the nearest coral skeleton. Therefore, the peripheries of all pore structures are lost due to their smaller values (rendered in yellow in Figure 3d). This immediately reveals the topology of a structure and areas with poor connectivity.

If the operation is conducted on the 3D size map, in which the peripherical voxels are also assigned with the pore size, the complete pore structure meeting the threshold value is retained. The visualization allows one to distinguish pore size by color brightness (Figure 3e).

3D visualization is produced via 3Dslicer, a free and open-source software platform for the visualization of medical, biological, and other 3D images (Fedorov et al., 2012). The ‘Volume Rendering’ module allows users to specify pore surface color with voxel value (which stores pore size), and therefore the 3D size of major pores, their 3D location or distribution, and connectivity are all visualized simultaneously. If the purpose is to visualize the average velocity of the fluid flow, one can multiply the matrix $\boldsymbol{A_3}$ by itself to obtain the square of the 3D size map in the visualization.

3. Methods for Anisotropy Characterization

Physical properties such as permeability and electrical resistivity have been proven to show anisotropy due to the anisotropy of the pore structure. Here, we take CT images of ice crystals as a demo to simultaneously depict the orientation and volume (or size) of individual ice crystals using color and color brightness.

3.1. Feature Identification of Individual Ice Crystals

The raw data in Figure 4a consists of CT images of a freezing salty sand specimen saturated with 5% KI solution. The ice nuclei in the pores are often platy and therefore have preferential growth orientations. The procedure for identifying crystal features is shown in Figure 4.

The identification of ice crystals anisotropy is carried out with ilastik. Crystals are isolated from segmented images to facilitate feature identification (Figure 4a). Here, orientations and volumes of ice crystals are selected to demonstrate their anisotropy. Specifically, crystal volumes are determined by corresponding voxel numbers, and Principal Component Analysis (Anderson, 1963) is employed for orientation characterization (Figure 4b). Three principal components corresponding to the long, medium, and short axes are obtained. The selection of feature principal components depends on the object shape and driven research questions. Given that the crystals are platy and thin along their short axes, we choose the third principal component, PC_3, which is perpendicular to the crystal's major plane, to visualize orientations. The identified ice crystals and obtained features of ice crystals serve as the input data for the subsequent color assignment. More details about the operation can be found at https://www.ilastik.org/documentation.

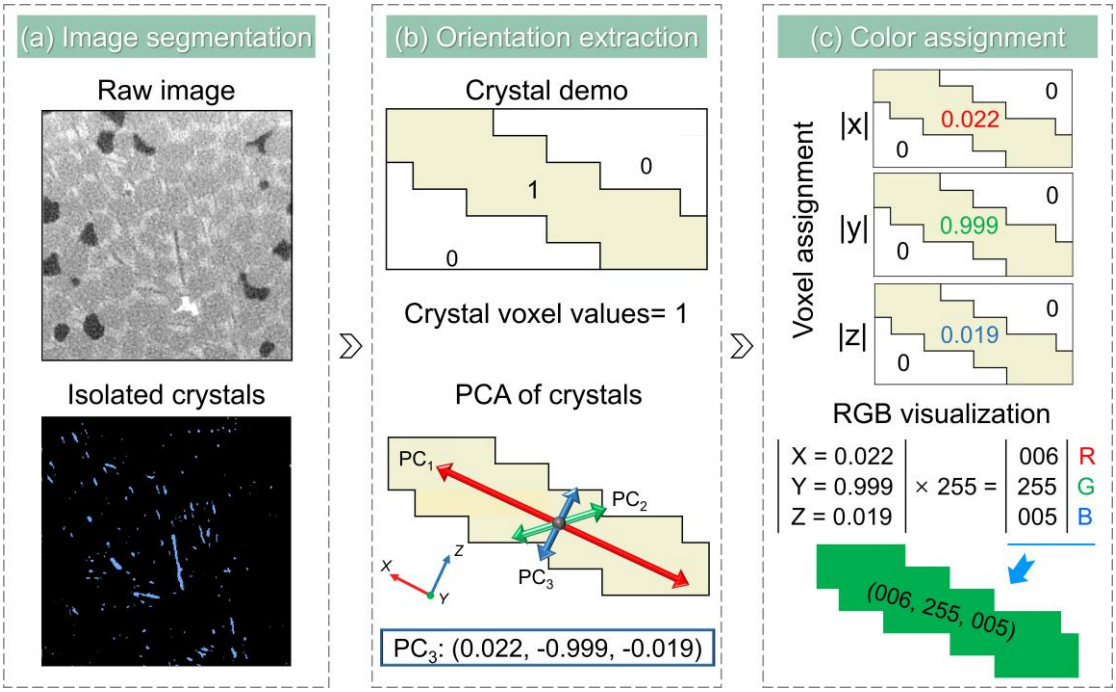

Figure 4. Ice crystal orientation identification and visualization. (a) Images segmentation. Isolated ice crystals segmented from a raw image. (b) Crystal orientation extracted by Principal Component Analysis (PCA). (c) Color assignments for crystal voxels based on the third principal component's $|x|$, $|y|$, and $|z|$ coordinates.

3.2. From Anisotropy to Color Assignment

The computed anisotropic features are now in the form of data. Here we propose a method to assign colors to the crystals according to their corresponding orientations. Three coordinates of the principal component PC_3 are mapped to three components in the RGB color system, which constructs various colors based on a combination of red, green, and blue. A normalization step is required to scale up the range of the three coordinates of PC_3 from [0, 1] to [0, 255] in the RGB system (Figure 4c). Note there could be negative values for the coordinates in a principal component, and 8 cases when considering the signs of the three coordinates can be reduced to 4 cases if we flip all the signs simultaneously to avoid negative z-axis coordinates as the orientation remains during this operation. Therefore, we can demonstrate the orientation of the crystals in a 3D view with four plots, in which the colors denote the orientations.

Considering that principal components are unit vectors with only two

independent variables, there is an additional variable left to present another feature of the crystals. Here we use the crystal size as an example. The crystal size is used to decide the modulus of the unit vector. Specifically, the three coordinates of unit vectors are linearly adjusted according to the volume ratio between the corresponding crystal and the largest crystal. So that the brightness of a certain color (or the combination of RGB) represents the crystal size, that is, larger crystals are brighter and smaller crystals are dimmer. In this way, both of the two features, orientations, and volume, are represented in the same 3D view. The volume used here could be replaced by elastic modulus, density, wave velocity, or anything else to demonstrate heterogeneity.

The color assignment is carried out with Matlab, and its pseudocode is given in Text S6 in Supporting Information. One example of this procedure is shown in Figure 4c. The voxels of ice crystals are assigned with $|x|$, $|y|$, or $|z|$ values of related vectors separately. At last, three files are computed and then imported into ImageJ to integrate them into one RGB file, where x, y, and z are replaced by one RGB value of the relevant crystal. The combined characteristics of orientations and volume of ice crystals are visually highlighted and classified in 3D view.

4. Results and Applications

This section uses three examples to show the visualization results and discusses how these visualizations enhance our understanding of the heterogeneity and anisotropy of porous media. These results are further used to generate a new approach to simplify geometric models in numerical simulations.

4.1. Coral Pore Structures

Understanding the flow paths within coral pore structures helps researchers comprehend carbon and nutrient cycling, as coral reefs are essential components in the biogeochemical cycle. The visualization of isolated coral pore structures is shown in Figure 5a. The intricate voids of coral gastrovascular canal system make it difficult

for researchers to extract the main branchlets (axial canal and lumen in calyx) from complex pore structures.

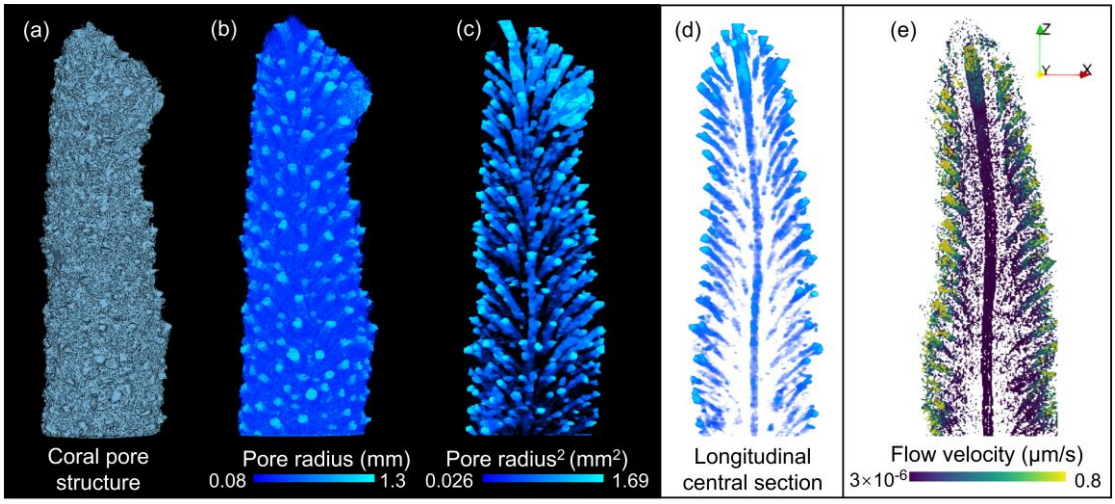

Figure 5. 3D visualization of the coral pore structure under various situations. (a) Isolated coral pore structure. (b) Color-coded visualization of coral pore size. (c) Extraction of coral main branches. (d) Intercepted central section of coral branches along the longitudinal plane, with a color-coded scale bar identical to that in (c). (e) Thresholded velocity distribution obtained by LBM to show main flow channels and velocities.

Figure 5b shows the visualization of the 3D pore size with the method in Section 2.4, in which false color is assigned to the voxels according to the pore size. The color varies from deep to light blue as pore size increases, therefore pore size can be distinguished by the color of the pore surface. One can roughly locate the major branchlets. We further filter pores smaller than a particular size by thresholding and denoising, and the branch distribution of the coral canal system is obtained (Figure 5c). The coral pore structure mainly consists of an axis channel and surrounding branchlets, resembling a tree. While all branchlets are connected to the main trunk in a tree structure, each branchlet in a coral system is relatively independent, with only small channels connecting with the axial canal. These small channels are filtered out during thresholding.

The visualization of the main branchlets of the coral pore structure not only helps to grasp the key heterogeneity but also sheds light on the hydrodynamic properties of the coral structure. According to Hagen-Poiseuille's equation, as also mentioned in Section 2.4, the average flow velocity in a round tube is proportional to the square of the tube diameter. Therefore, for comparison with the later obtained flow velocity, we present the values of R^2 here. The fluid flow within the coral sample, driven by ocean currents, is simulated with the Lattice Boltzmann Method (LBM), and the simulated boundary conditions are detailed in Table S1 and Figure S2 in Supporting Information. In Figure 5d, at the periphery of the branchlets, the pore size reaches its maximum, and the flow velocity also reaches the largest in Figure 5e. In the area with a larger aperture, the simulation results show a larger flow rate. Therefore, the distribution of flow velocity can be predicted with the color-coded pore size.

One of the key advantages of the visualization lies in its efficiency in extracting main flow paths through porous media and its scale independence compared with numerical simulations. The coral pore structures contain a large number of tiny pores in addition to the tree-shaped branches, and including these tiny pores in the simulation greatly increases the computational cost because a large number of grid cells are required. Due to the large data size, model simplification is frequently required. For studies that prefer to preserve the entire structure, researchers often need to ignore certain details of the reconstructed model by sacrificing the resolution to shorten the computational time, which retains the physical size of the model but uses a coarser mesh. For the proposed method, as long as the resolution of the image is sufficient, the results we obtain cover all details. Comparatively, the computational cost of the full-resolution image with our method is still 1/100 of the fluid dynamic simulation (LBM simulation used here) with a quarter reduced resolution. The prompt analyses, purely based on geometry, although simple, could greatly help our understanding of the pore structure by identifying the skeleton as the main contributor to the flow. Furthermore, these analyses do not rely on computing power and therefore

394 can be applied to a large area. In addition, it is easy to conduct such analyses on
395 different portions of porous media and merge the results afterward, while a similar
396 approach with LBM simulation is not applicable.

397 **4.2. Fractured Rock**

398 Identification of preferential flow channels in rock masses and sediments is
399 universally required in geological engineering. Here we take fractured rock as
400 examples to demonstrate the application of our method in preferential flow channels
401 extraction. Preferential flow channels here are defined by the seepage characteristics
402 of good connectivity and high fracture apertures.

403 A rock sample and fracture details are shown in Figure 6a. The omnidirectional
404 fracture network extracted from CT images makes it difficult to determine the
405 preferential seepage path without further processing (Figure 6c). Preferential flow
406 channels are positively correlated with the aperture and connectivity of fractures.
407 According to Hagen-Poiseuille's equation, the flow velocity in planar flow channels is
408 proportional to R, and the volume flow is proportional to R^3. Therefore, the quantitive
409 analysis of fracture aperture distribution in rock sample based on 3D size
410 determination algorithm is critical.

411

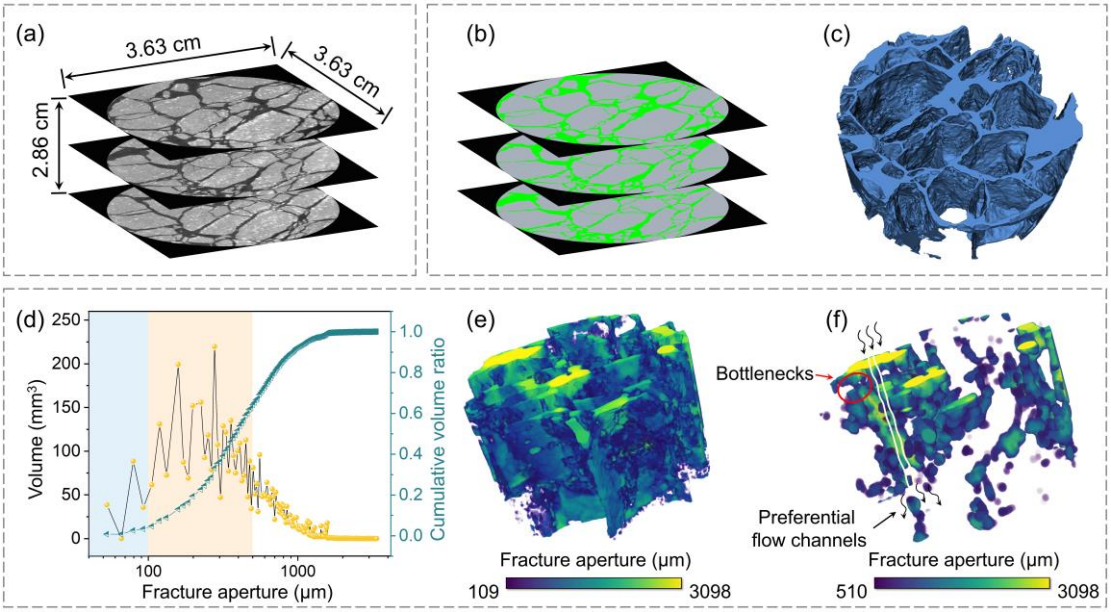

Figure 6. Details of the fractured rock sample and its connectivity visualization. (a) Rock sample size and its raw CT images. (b) Segmented images. The gray and green phases are rock and fracture. (c) 3D fracture structures. (d) The distribution of fracture apertures. (e, f) 3D visualization of remaining fracture structure after excluding pores less than 100 and 500 μm. 100 μm has little effect on the whole structure connectivity, while 500 μm is the maximum threshold value before connectivity is lost.

The fracture aperture shows obvious heterogeneity, as shown in Figure 6d, and small pore throats are common, which can be the bottleneck that limits the flow continuity. To identify the size of the pore throats that would affect the fracture network connectivity, we use different threshold values on the full fracture network and identify the exact location of the pore throats. When pores with radius less than 100 μm are hidden, the connectivity of the fracture network is not greatly affected (Figure 6e). However, when the threshold value is up to 500 μm, the connectivity of the fracture network deteriorates significantly, and one bottleneck appears (circled in red in Figure 6f). There is still one large aperture area marked in black that remains connected vertically, indicating its major contribution to the flow. We consider the preferential flow channels as the remaining fracture network.

Additional permeability analyses of the rock sample with Avizo are carried out to

verify the reliability of identified preferential flow channels with fractures larger than 500 μm, and the results are given in Text S7 in Supporting Information. The results prove the effectiveness of this method in predicting preferential flow channels, and the velocities at different locations can also be roughly compared with fracture color representing aperture.

4.3. Ice Crystals

Symmetry breaking occurs during crystallization. The formed crystals frequently show directional behavior. Anisotropy of crystals results in directional-dependent strength, stiffness, and deformation characteristics. Revealing crystal orientations within a rock can help us interpret its anisotropic properties. We use ice crystal formation in a salty sandy specimen as an example. Ice crystal images used here are from the nucleation stage, revealing crystal orientations that can help us understand the nuclei growth preference (Anderson et al., 2017).

Rose diagram and equal-area stereographic projection are used first to show the statistics of crystal orientations (Figure 7). A significant number of dip angles around 0º indicates the crystals show a preferential growth orientation along vertical directions (note that the axis perpendicular to the crystal major plane is selected to demonstrate the crystal orientation). In Figure 7b, the semi-sphere is expanded to a 2D plane according to equal-area stereographic projection (Text S8 in Supporting Information). Equal-area is chosen so that the density in Figure 7b (shown as cloud colors), defined as the number of crystals per unit area, demonstrates the probability of crystal orientations. The color bar encodes the point density in the subregion, which also represents the probability of crystal orientations. The main orientation is easily visible as yellow areas, which represent a strong prevalence along the horizontal axis, and the central high density is caused by its relatively small equal area. Additionally, it correlates the volume of each crystal with the size of the dot. Crystals with volumes bigger than 1000 voxels are all set as 1000 voxels, so that there are no abnormal dots overlapping with adjacent smaller dots.

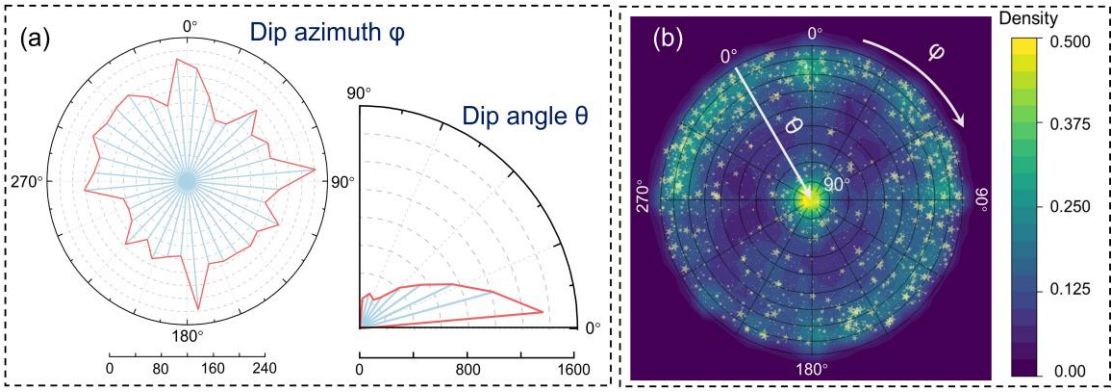

Figure 7. Statistic of crystal orientation distributions. (a) Rose diagram. The dip azimuth φ ranges from 0º to 360º. The dip angle θ ranges from 0º (horizontal) to 90º (vertical), showing the angle inclined from the horizontal plane. (b) Equal-area stereographic projection. The dip azimuth φ and dip angle θ correspond to that in (a).

In this method, the correspondences between features and the crystals are missing. All crystals are gathered at the same origin, and the original location of each crystal, along with the relative position between different crystals, is not available. Besides, the morphology of the crystal, as a key anisotropic characteristic, is absent. We show both the morphology, spatial distribution, and orientation of all crystals in one visualization (Figure 8a) and further correlate the color brightness with the crystal size in Figure 8b, where the brightness of the color demonstrates the crystal size (See 3D animations in Data Set S1 in Supporting Information). Here, the maximum volume is set as 500 voxels to avoid extensive crystal darkening. Crystals larger than 500 voxels maintain their original color, while those smaller than 500 voxels appear dimmer. The crystal size shown as the color brightness can be replaced by another characteristic when necessary. For example, it can be either fracture aperture, length, or aspect ratio in geology.

We plot the color coding overlapping the stereographic projection orientations in the center of the four quadrants (Figure 8). One can then look for the orientation of a particular crystal according to its color and correspondingly find its dip angle and dip azimuth. The group behavior among homooriented crystals is clearly identified, with the major vertically orientated crystals (crystals with color ranging between red and

green in Figure 8) spreading across other regions. This indicates that the nuclei prefer to grow along the z-axis, aligning with the direction of the temperature gradient, while the minority of blue crystals accumulate at the side corner. Such a trend would not be possible to discern in a stereographic projection plot, which, in turn, highlights the necessity of the proposed 3D visualization.

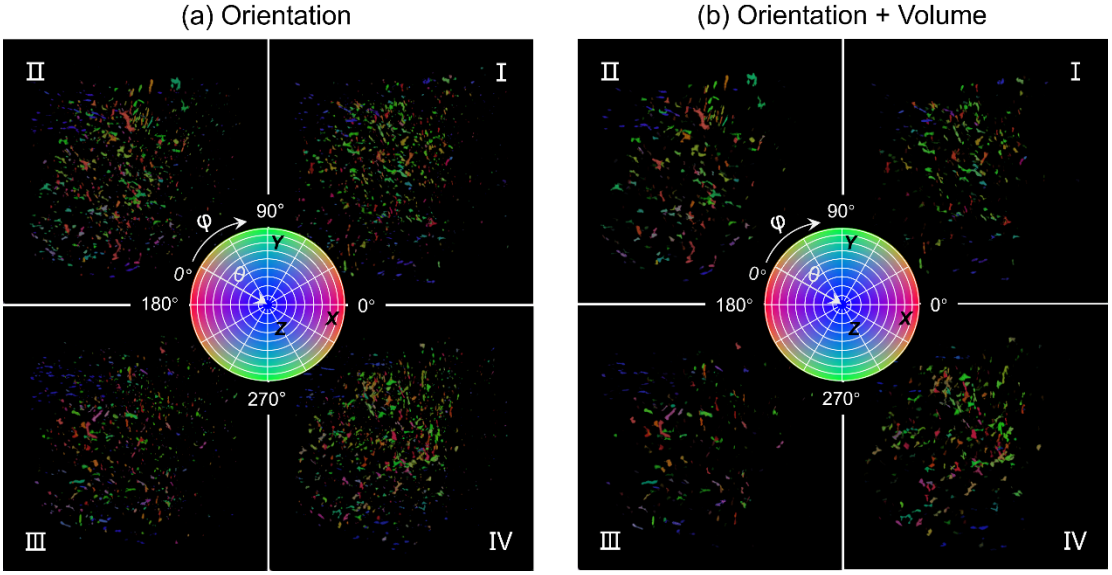

Figure 8. Visualization of anisotropic characteristics of ice crystals with four quadrants (a) Orientation visualization. (b) Simultaneous visualization of orientation and volume. Red, green, and blue colors signify x, y, and z coordinates of vectors, respectively. Various colors are generated by blending these three primary colors according to their corresponding vector coordinates. This integration process produces a spectrum of colors, which is presented in the form of equal-area stereographic projection. Each color represents a unique orientation, and the determination of orientation follows the illustration in Figure 7.

We have compared this method with those found in the literature across fields including fiber-reinforced composites, geology, and crystallography. Mishurova et al. (2017) presented the orientation of fibers by two plots to separately demonstrate the azimuth angle and dip angle. In crystallography, the most well-known color coding is the crystal orientation map, which also needs two plots to identify one direction

(Wittwer & Seita, 2022). Therefore, it is difficult to grasp the orientation directly in these two methods. Robb et al. (2007) used a color sphere based on a combination of the azimuth angle and dip angle. Weissenböck et al., (2014) used the same color map as us but did not divide it into four cases. However, in both of these two methods, specific colors could represent more than one orientation, and sometimes the orientation difference between two features shown with the same color could be more than 90 degrees. In comparison, our method demonstrates the direction in just one plot, and a unique direction could be traced to one color in one of the four quadrants. The three colors RGB naturally align with the x, y, and z directions, which makes it a natural match with the Cartesian coordinate system and, therefore, more intuitive. In addition, we combine size or any other heterogeneity with orientation in just one plot, a feature not available in existing methods.

4.4. Geometrical Model Simplification for Numerical Simulation

Previous sections have demonstrated the effectiveness of our method in enhancing the understanding of porous media heterogeneity and anisotropy. Based on this understanding, we further discuss its potential for geometrical model simplification in the numerical simulation.

The fluid flow simulation results of the coral sample show that the filtered tiny pores have little influence on the ultimate flow properties of the coral pore structure, as discussed in Section 4.1. This provides a new approach to simplify the geometric model by filtering out tiny pores at the periphery of the coral structure, which can greatly improve computational efficiency without losing reliability. The simplest way is to use only the main branchlets of the coral pore structure; however, the central canal is disconnected from the branchlets. Therefore, we purposely retained the small pores around the central canal to ensure connectivity. As shown in Figure 9g, the central canal is dilated M times, connecting all the branchlets, the Boolean conjunction of the dilated central canal and the branchlets defines the region (labeled as the identified region) in which all inner pores should be included in the simulation. Such an approach guarantees a good connectivity among all the main channels while

involves only a small number of small pores.

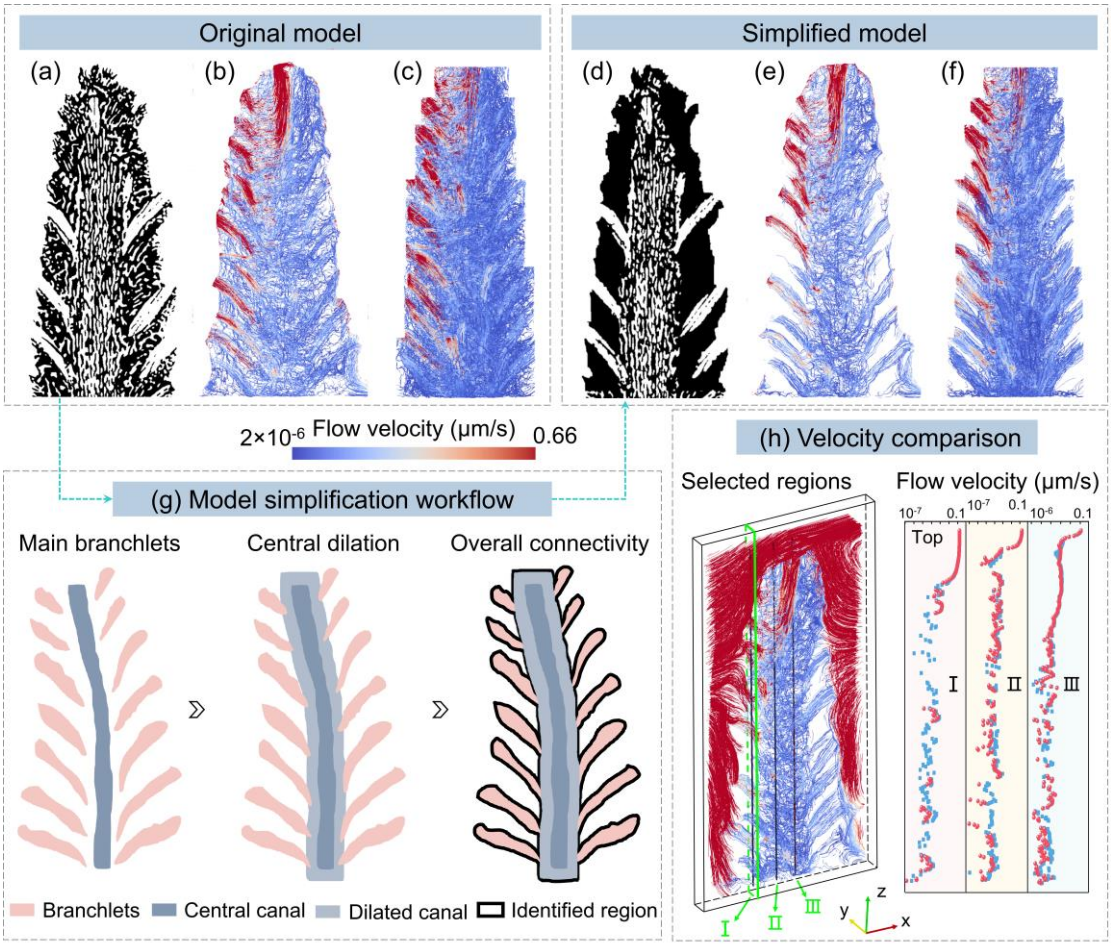

Figure 9. Comparison of simulation results before and after the coral pore structure simplification. (a, d) Original and simplified simulation models. The black phase represents the coral skeleton. (b, e) The longitudinal section of streamline distribution. (c, f) Overall streamline distribution in 3D. (g) Workflow of coral pore structure simplification. (h) Flow velocities pre- and post-simplification (plotted as blue and red dots) at three selected regions (labeled I, II, and III).

The same fluid flow conditions are applied to both the original and simplified models. Simulation results of the simplified model preserve fluid flow channels (Figures 9b, e) and present clearer streamlines (Figures 9c, f). Overall, the absence of tiny pores slightly changes the absolute velocity (less than 5% for the average flow velocity: 1.1%, 2.5%, and 5% for regions I, II, and III) and flow paths (which are

more aligned with branch boundaries), and the flow velocity distribution remains consistent with the original model (Figure 9h). The effect of simplification on the flow field outside the coral is even less as the velocity profile at the top in Figure 9h pre- and post- simplification almost overlap with each other.

Taking the rock sample in Figure 6 as an example, fractures narrower than a certain threshold value are hidden and then the permeability of the remaining fracture structure and the computation time are calculated with COMSOL. As the omitting threshold increases, more fractures are neglected in the simulation, therefore, the retained permeability, voxel count, and CPU time all decrease. The effect of these filtered fractures on the overall permeability is equivalent to the reduction ratio of overall permeability, and the results are shown in Figure 10. The fractures below 100 μm have little effect on the overall permeability, and then the permeability sharply decreases with the increasing threshold value. Another sand specimen (Figure 10b) is used to verify this approach (more details about this specimen are given in Text S9 in Supporting Information). When a threshold value smaller than 33 μm is applied, the reduction in overall permeability is less than 3%.

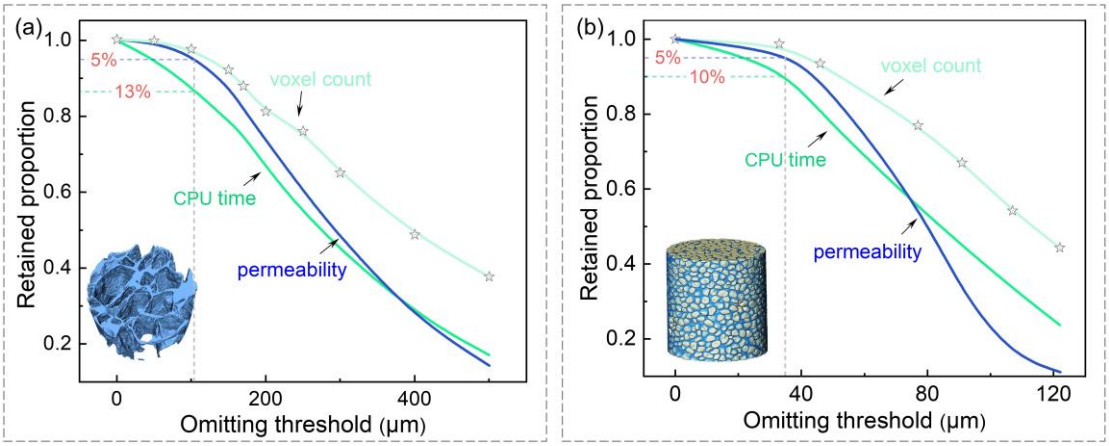

Figure 10. Retained proportion of permeability, surface area, and voxel count over the total while omitting pores smaller than a certain threshold, as well as the corresponding CPU time ratio over the case with the original pore structure. (a) Rock sample. (b) Saturated sand specimen.

The voxel count and surface area of the pore structure are correlated to the complexity of the mesh and computational cost. It is reported that there is an approximate power law relationship between CPU time and the number of finite elements, with an exponent larger than 1.5 (Erhel et al., 2009). Here, voxelized models are applied for permeability simulation. Consequently, the computation time obtained (dark green line) shows a direct correlation with voxel count (light green line), following a quadratic function with an exponent of about 2. If we regard a 5% permeability loss as acceptable, the CPU time can be reduced by 13% and 10% for the rock and sand cases, respectively. This reduction in computational time works for both samples. Therefore, fractures with low contributions (100 and 35 μm for the specific rock and sand specimens) can be identified in advance with our method to simplify the fracture structures during simulation modeling and further enhance computational efficiency.

Simply neglecting smaller pores can cause problems in multiphase flow in porous media, since the neglected pores could be occupied by the wetting phase. On the other hand, we could consider the smaller pores and the simplified pore structure separately. For example, in a capillarity regime, we could assume that the wetting phase is stuck in the small pores and not sensitive to the pressure gradient, while still responding to other physical processes such as diffusion.

5. Conclusions

This study proposes a cost-effective method for simultaneously demonstrating heterogeneity and anisotropy based on geometry and image analyses.

The heterogeneity of porous media is characterized by measuring pore size in CT images, and the anisotropy is determined using principal component analysis. Then a simultaneous visualization of both the orientation-based anisotropy and the size-based heterogeneity is generated by rendering the pore structure surface using color and color brightness. This visualization preserves the morphology and spatial location of pore structure, which enables interactive exploration of the spatial relationships

between individual pores. Furthermore, we propose a refined stereographic projection to statistically display both anisotropy (orientation) and heterogeneity (size) in one plot.

The proposed method facilitates our understanding of heterogeneity and anisotropy within the porous media, and a general trend for size-related physical behavior can be predicted with the visualization results. We then propose a method of geometrical model simplification for the numerical simulation, specifically, by discarding tiny pores with low contribution to property while retaining the major contributing structures. The simplified models yield a good match with the original model but significantly reduce the computational cost.

Acknowledgments

This work is supported by Research Center for Industries of the Future (RCIF), Westlake Education Foundation, and Open Research Fund of State Key Laboratory of Geomechanics and Geotechnical Engineering, Institute of Rock and Soil Mechanics, Chinese Academy of Sciences (Grant No. SKLGME021008). We thank Westlake Center for Micro/Nano Fabrication for the facility support and technical assistance.

Open Research

The CT image data and corresponding image processing results in this study are available at Tian (2023) in Mendeley Data via https://doi.org/10.17632/6ypbv8gbcp.1. The code associated to this work is archived and published as Yin (2023) in Mendeley Data via https://doi.org/10.17632/rbgwgc2yv9.1, which can be accessed freely after registration. The LBM simulation and the corresponding model were described in MechSys (2021): Multi-physics Simulation Library and Galindo-Torres (2013). The software can be obtained from http://mechsys.nongnu.org/.

References

Anderson, M. W., Gebbie-Rayet, J. T., Hill, A. R., Farida, N., Attfield, M. P., Cubillas, P., et al. (2017). Predicting crystal growth via a unified kinetic three-dimensional partition model. *Nature*, *544*, 456–459. https://doi.org/10.1038/nature21684

Anderson, T. W. (1963). Asymptotic theory for principal component analysis. *Annals of mathematical statistics*, *34*(1), 122–148. https://doi.org/10.1214/aoms/1177704248

Bang, B., & Lukkassen, D. (1999). Application of homogenization theory related to Stokes flow in porous media. *Application of Mathematics*, *44*(4), 309–319. https://doi.org/10.1023/A:1023084614058

Berg, S., Kutra, D., Kroeger, T., Straehle, C. N., Kausler, B. X., Haubold, C., et al. (2019). ilastik: interactive machine learning for (bio) image analysis. *Nature Methods*, *16*, 1226–1232. https://doi.org/10.1038/s41592-019-0582-9

Budinger, T. F., & Lauterbur, P. C. (1984). Nuclear magnetic resonance technology for medical studies. *Science*, *226*, 288–298. http://dx.doi.org/10.1126/science.6385252

Bultreys, T., Van Hoorebeke, L., & Cnudde, V. (2016). Simulating secondary waterflooding in heterogeneous rocks with variable wettability using an image-based, multiscale pore network model. *Water Resources Research*, *52*(9), 6833–6850. https://doi.org/10.1002/2016WR018950

Chandra, R., Dagum, L., Kohr, D., Menon, R., Maydan, D., & McDonald, J. (2001). Parallel programming in OpenMP. San Francisco, Morgan Kaufmann Publishers Inc.

Chen, J., Yang, S., Mei, Q., Chen, J., Chen, H., Zou, C., et al. (2021). Influence of pore structure on gas flow and recovery in ultradeep carbonate gas reservoirs at multiple scales. *Energy & Fuels*, *35*(5), 3951–3971. https://doi.org/10.1021/acs.energyfuels.0c04178

644 Chong, Z., Li, X., Chen, X., Zhang, J., & Lu, J. (2017). Numerical investigation into
645 the effect of natural fracture density on hydraulic fracture network propagation.
646 *Energies*, *10*, 914. https://doi.org/10.3390/en10070914
647 Degu, A. M., & Hossain, F. (2012). Investigating the mesoscale impact of artificial
648 reservoirs on frequency of rain during growing season. *Water Resources*
649 *Research*, *48*(5), W25510. https://doi.org/10.1029/2011WR010966
650 Erhel, J., De Dreuzy, J. R., & Poirriez, B. (2009). Flow simulation in
651 three-dimensional discrete fracture networks. *SIAM Journal on Scientific*
652 *Computing*, *31*(4), 2688–2705. https://doi.org/10.1137/080729244
653 Fatt, I. (1956). The network model of porous media I. Capillary pressure
654 characteristics. *Transaction of the AIME*, *207*(1), 144 – 159.
655 https://doi.org/10.2118/574-G
656 Fedorov, A., Beichel, R., Kalpathy-Cramer, J., Fine, J., Fillion-Robin, J., Pujol, S., et
657 al. (2012). 3D Slicer as an Image Computing Platform for the Quantitative
658 Imaging Network. *Magnetic Resonance Imaging*, *30*(9), 1323–1341.
659 https://doi.org/10.1016/j.mri.2012.05.001
660 Ferreira, A. A. S., & Nick, H. M. (2023). Computed-tomography-based discrete
661 fracture-matrix modeling: An integrated framework for deriving fracture
662 networks. *Advances in Water Resources*, *177*, 104450.
663 https://doi.org/10.1016/j.advwatres.2023.104450
664 Flannery, B. P., Deckman, H. W., Roberge, W. G., & D'Amico, K. L. (1987).
665 Three-dimensional X-ray microtomography. *Science*, *237*, 1439–1444.
666 http://dx.doi.org/10.1126/science. 237.4821.1439
667 Galindo-Torres, S. A., Scheuermann, A., & Li, L. (2012). Numerical study on the
668 permeability in a tensorial form for laminar flow in anisotropic porous media.
669 *Physical Review E*, *86*, 046306. https://doi.org/10.1103/PhysRevE.86.046306
670 Galindo-Torres, S. A. (2013). A coupled discrete element lattice Boltzmann method
671 for the simulation of fluid-solid interaction with particles of general shapes.

Computer Methods in Applied Mechanics and Engineering, *265*, 107–119. https://doi.org/10.1016/j.cma.2013.06.004

Grau, S., Verges, E., Tost, D., & Ayala, D. (2010). Exploration of porous structures with illustrative visualizations. *Computers & Graphics-UK*, *34*(4), 398–408. http://dx.doi.org/10.1016/j.cag.2010.05.001

Grevera, G.J. (2007). Distance transform algorithms and their implementation and evaluation. Deformable Models: Biomedical and Clinical Applications, Springer New York, New York, NY, 33–60.

Hilderand, T., & Ruegsegger, P. (1997). A new method for the model-independent assessment of thickness in three-dimensional images. *Journal of Microscopy*, *185*, 67–75. https://doi.org/10.1046/j.1365-2818.1997.1340694.x

Howarth, R. J. (1996). History of the stereographic projection and its early use in geology. *Terra Nova*, *8*(6), 499–513. https://doi.org/10.1111/j.1365-3121.1996.tb00 779.x

Hunt, A. G., & Sahimi, M. (2017). Flow, transport, and reaction in porous media: Percolation scaling, critical-path analysis, and effective medium approximation. *Reviews of Geophysics*, *55*, 993–1078. https://doi.org/10.1002/2017RG000558

Hyman, J. D. (2020). Flow channeling in fracture networks: characterizing the effect of density on preferential flow path formation. *Water Resources Research*, *56*(9), e2020WR027986. https://doi.org/10.1029/2020WR027986

Ihli, J., Jacob, R.R., Holler, M., Guizar-Sicairos, M., Diaz, A., da Silva, J. C., et al. (2017). A three-dimensional view of structural changes caused by deactivation of fluid catalytic cracking catalysts. *Nature Communications*, *8*, 809. https://doi.org/10.1038/s41467-017-00789-w

Jiang, Z., van Dijke, M. I. J., Geiger, S., Ma, J., Couples, G. D., & Li, X. (2017). Pore network extraction for fractured porous media. *Advances in Water Resources*, *107*, 280–289. https://doi.org/10.1016/ j.advwatres.2017.06.025

699 Jiang, Z., van Dijke, M. I. J., Sorbie, K. S., & Couples, G. D. (2013). Representation
700 of multiscale heterogeneity via multiscale pore networks. *Water Resources*
701 *Research*, *49*(9), 5437–5449. https://doi.org/10.1002/wrcr.20304
702 Jing, Y., Armstrong, R. T., & Mostaghimi, P. (2020). Image-based fracture pipe
703 network modelling for prediction of coal permeability. *Fuel*, *270*(*15*), 117447.
704 https://doi.org/10.1016/j.fuel.2020.117447
705 Johnson, G. R., Gupta, K., Putz, D. K., Hu, Q., & Brusseau, M.L. (2003). The effect
706 of local-scale physical heterogeneity and nonlinear, rate-limited
707 sorption/desorption on contaminant transport in porous media. *Journal of*
708 *Contaminant Hydrology*, *64*(1-2), 35–58.
709 https://doi.org/10.1016/S0169-7722(02)00103-1
710 Lee, T., Kashyap, R., & Chu, R. (1994). Building skeleton models via 3-D medial
711 surface axis thinning algorithms. *CVGIP: Graphical Models and Image*
712 *Processing*, *55*(6), 462-478. https://doi.org/10.1006/cgip.1994.1042
713 Li, Y., Liao, X., He, C., & Lu, Z. (2021). Calcium transport along the axial canal in
714 Acropora. *Diversity*, *13*(9), 407. https://doi.org/10.3390/d13090407
715 Lyu, Q.F., Wu, H., & Li, X. (2021). A 3D model reflecting the dynamic generating
716 process of pore networks for geological porous media. *Computers and*
717 *Geotechnics*, *140*, 104444. https://doi.org/10.1016/j.compgeo.2021.104444
718 Mahabadi, N., Zheng, X., Yun, T. S., van Paassen, L., & Jang, J. (2018). Gas bubble
719 migration and trapping in porous media: pore-scale simulation. *Journal of*
720 *Geophysical Research: Solid Earth*, *123*(2), 1060–1071.
721 https://doi.org/10.1002/2017JB015331
722 Martin-Garin, B., Lathuilière, B., Verrecchia, E. P., & Geister, J. (2007). Use of
723 fractal dimensions to quantify coral shape. *Coral Reefs*, *26*, 541–550.
724 https://doi.org/10.1007/s00338-007-0256-4
725 Merchant, F. A., Shah, S. K., & Castleman, K. R. (2023). Chapter Eight-Object
726 Measurement. *Microscope Image Processing (Second Edition)*, 153–175.
727 https://doi.org/10.1016/B978-0-12-821049-9.00017-4

Mishurova, T., Léonard, F., Oesch, T., Meinel, D., Bruno, G., Rachmatulin, N., et al. (2017). *Evaluation of fiber orientation in a composite and its effect on material behavior*. Paper presented at 7th Conference on Industrial Computed Tomography, Leuven, Belgium.

Nemati, R., Shahrouzi, J. R., & Alizadeh, R. (2020). A stochastic approach for predicting tortuosity in porous media via pore network modeling. *Computers and Geotechnics*, *120*, 103406. https://doi.org/10.1016/j.compgeo.2019.103406

Nemec, W. (1988). The shape of the rose. *Sedimentary Geology*, *59*, 149–152. https://doi.org/10.1016/0037-0738(88)90105-4

Puyguiraud, A., Gouze, P., & Dentz, M. (2020). Is there a representative elementary volume for anomalous dispersion? *Transport in Porous Media*, *131*(2), 767–778. https://doi.org/ 10.1007/s11242-019-01366-z

Qin, X., Cai, J., & Wang, G. (2023). Pore-scale modeling of pore structure properties and wettability effect on permeability of low-rank coal. *International Journal of Mining Science and Technology*, *33*(5), 573–584. https://doi.org/10.1016/j.ijmst.2023.02.005

Ren, X., & Santamarina, J. C. (2018). The hydraulic conductivity of sediments: Apore size perspective. *Engineering Geology*, *233*(31), 48–54. https://doi.org/10.1016/j.enggeo.2017.11.022

Robb, K., Wirjadi, O., & Schladitz, K. (2007). *Fiber Orientation Estimation from 3D Image Data: Practical Algorithms, Visualization, and Interpretation.* Paper presented at 7th International Conference on Hybrid Intelligent Systems, Kaiserslautern, Germany.

Schindelin, J., Arganda-Carreras, I., Frise, E., Kaynig, V., Longair, M., Pietzsch, T., et al. (2012). Fiji: An Open-Source Platform for Biological-Image Analysis. *Nature Methods*, *9*, 676–682. https://doi.org/10.1038/nmeth.2019

Sebben, M. L., & Werner, A. D. (2016). A modeling investigation of solute transport in permeable porous media containing a discrete preferential flow feature.

Advances in Water Resources, *94*, 307–317. https://doi.org/10.1016/j.advwatres.2016.05.022

Shahriar, M. F., & Khanal, A. (2023). Effect of formation heterogeneity on CO_2 dissolution in subsurface porous media. *ACS Earth and Space Chemistry*, *7*(10), 2073–2090. https://doi.org/10.1021/acsearthspacechem.3c00175.

Shigorina, E., Rüdiger, F., Tartakovsky, A. M., Sauter, M., & Kordilla, J. (2021). Multiscale Smoothed Particle Hydrodynamics Model Development for Simulating Preferential Flow Dynamics in Fractured Porous Media. *Water Resources Research*, *57*(3), e2020WR027323. https://doi.org/10.1029/2020WR027323

Silin, D., & Patzek, T. (2006). Pore space morphology analysis using maximal inscribed spheres. *Physica A: Statistical Mechanics and its Applications*, *371*(2), 336–360. https://doi.org/10.1016/j.physa.2006. 04.048

Song, W., Jun, Y., Wang, D., Li, Y., Sun, H., & Yang, Y. (2020). Dynamic pore network modelling of real gas transport in shale nanopore structure. *Journal of Petroleum Science and Engineering*, *184*, 106506. https://doi.org/10.1016/j.petrol.2019.106506

Van der Walts, S., Schönberger J. L., Nunez-Iglesias J., Boulogne F., Warner J. D., Yager N., Gouillart E., & Yu T. (2014). scikit-image: Image processing in Python Peer J 2:e453. https://doi.org/10.7717/peerj.453

Wang, J., Huang, X., Xu, J. Zhang, Z., Wang, S. F., & Li, Y. (2023). Network analysis of pore structure of coral reef limestone and its implications for seepage flow. *Engineering Geology*, *318*(5), 107103. https://doi.org/10.1016/j.enggeo.2023.107103

Weissenbock, J., Amirkhanov, A., Li, W., Reh, A., Amirkhanov, A., Groller, E., et al. (2014). *FiberScout: An Interactive Tool for Exploring and Analyzing Fiber Reinforced Polymers*. Paper presented at 2014 IEEE Pacific Visualization Symposium. Yokohama, Japan.

Wildenschild, D., & Sheppard, A. P. (2012). X-ray imaging and analysis techniques for quantifying pore-scale structure and processes in subsurface porous medium systems. *Advances in Water Resources*, *51*, 217–246. http://dx.doi.org/10.1016/j.advwatres.2012. 07.018.

Wittwer, M., & Seita, M. (2022). A machine learning approach to map crystal orientation by optical microscopy. *npj Computational Materials, 8*(8). https://doi.org/10.1038/s41524-021-00688-1

Xu, L., Myers, M., Li, Q., White, C., & Zhang, X. (2020). Migration and storage characteristics of supercritical CO_2 in anisotropic sandstones with clay interlayers based on X-CT experiments. *Journal of Hydrology*, *580*, 124239. https://doi.org/10.1016/j.jhydrol.2019.124239

Yang, Z., Xu, T., Wang, F., Yang, Y., Li, X., & Zhao, N. (2018). Impact of inner reservoir faults on migration and storage of injected CO_2. *Internal Journal of Greenhouse Gas Control*, *72*, 14–25. https://doi.org/10.1016/j.ijggc.2018.03.006

Zhang, K., Wang, S., Wang, L., Cheng, Y., Li, W., & Han, X. (2022). 3D visualization of tectonic coal microstructure and quantitative characterization on topological connectivity of pore-fracture networks by Micro-CT. *Journal of Petroleum Science and Engineering*, *208*, 109675. https://doi.org/10.1016/j.petrol.2021.109675

Zhang, Z., Li, C., Ning, F., Liu, L., Cai, J., Liu, C., et al. (2020). Pore Fractal Characteristics of Hydrate-Bearing Sands and Implications to the Saturated Water Permeability. *Journal of Geophysical Research: Solid Earth*, *125*(3), e2019JB018721. https://doi.org/10.1029/2019JB018721

Figure 1.

(a)

Axial canal

(b)

1 mm

Defect

(c)

2 mm

Gastrovascular
canal system

(d)

2 mm

Lumen in calyx

5 mm

Figure 2.

(a) Raw image

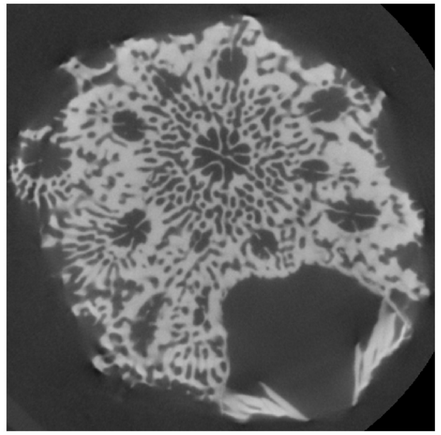

(b) Segmentation

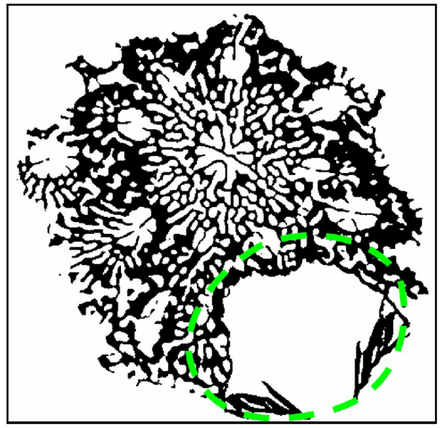

(c) Fill holes

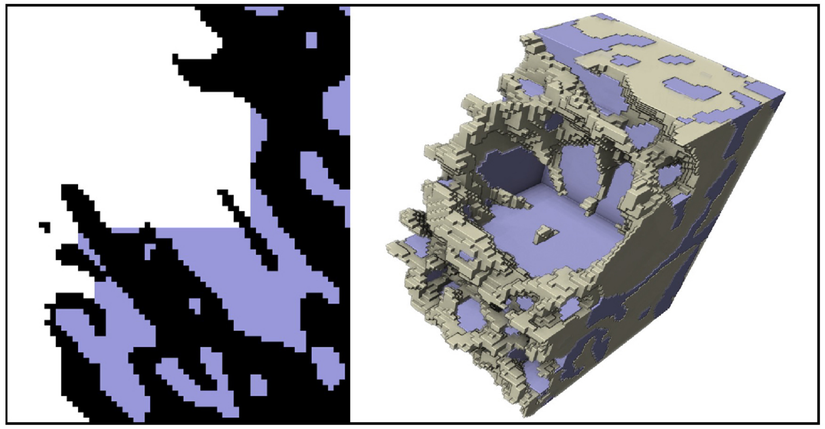

(d) Dilate & erode + fill holes

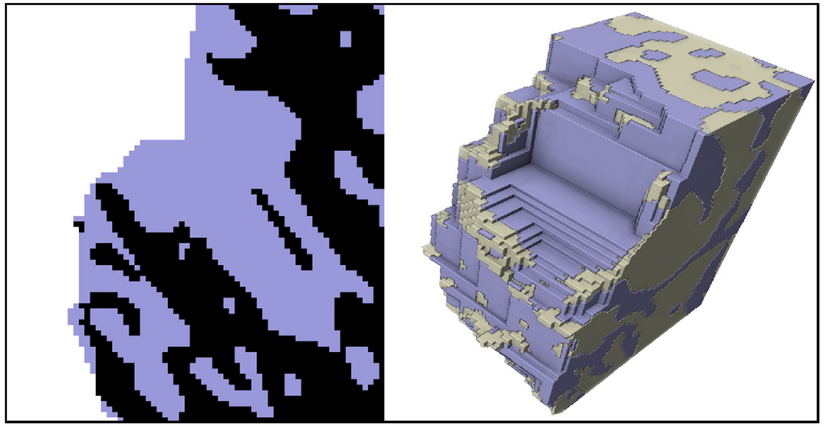

(e) Dilate

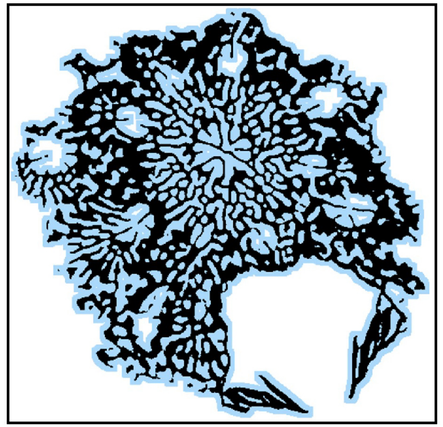

(f) Erode

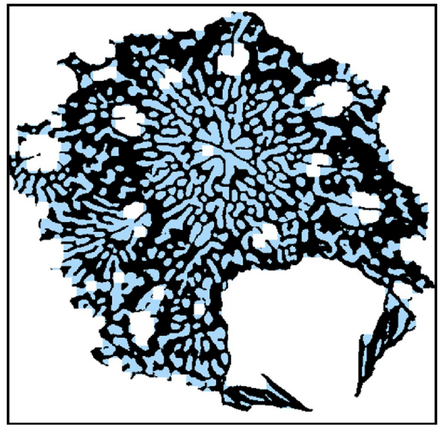

(g) Isolated pores

Dilate & Erode
+ fill hole

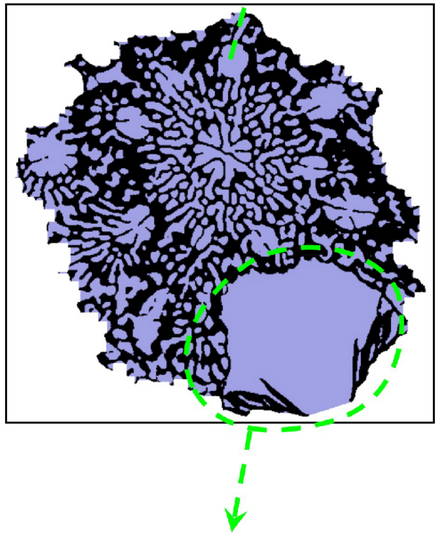

Manually closed
+ fill hole

Figure 3.

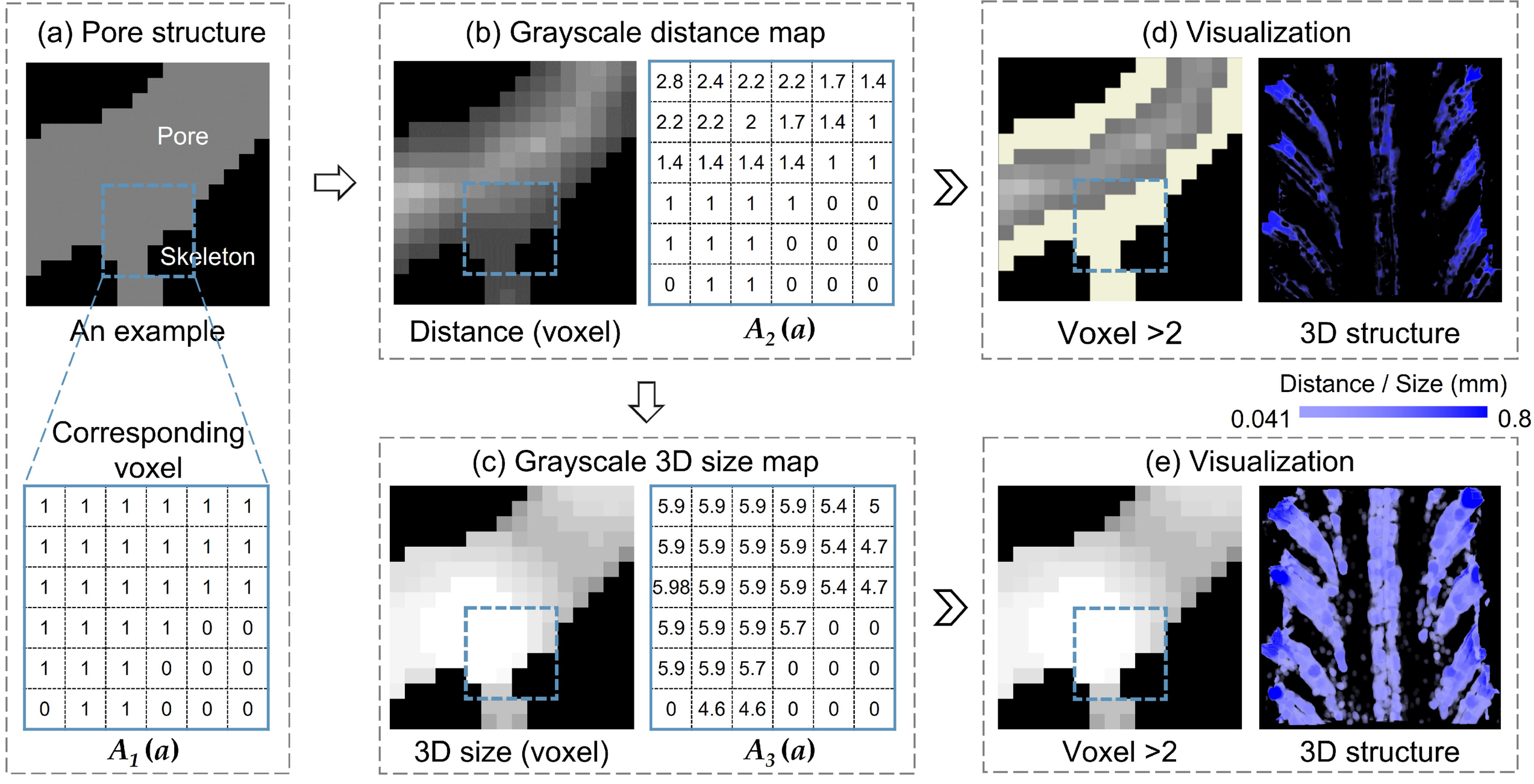
(a) Pore structure
Pore
Skeleton
An example
Corresponding voxel
1 1 1 1 1 1
1 1 1 1 1 1
1 1 1 1 1 1
1 1 1 1 0 0
1 1 1 0 0 0
0 1 1 0 0 0
$A_1(a)$
(b) Grayscale distance map
2.8 2.4 2.2 2.2 1.7 1.4
2.2 2.2 2 1.7 1.4 1
1.4 1.4 1.4 1.4 1 1
1 1 1 1 0 0
1 1 1 0 0 0
0 1 1 0 0 0
Distance (voxel)
$A_2(a)$
(c) Grayscale 3D size map
5.9 5.9 5.9 5.9 5.4 5
5.9 5.9 5.9 5.9 5.4 4.7
5.98 5.9 5.9 5.9 5.4 4.7
5.9 5.9 5.9 5.7 0 0
5.9 5.9 5.7 0 0 0
0 4.6 4.6 0 0 0
3D size (voxel)
$A_3(a)$
(d) Visualization
Voxel >2
3D structure
Distance / Size (mm)
0.041
0.8
(e) Visualization
Voxel >2
3D structure

Figure 4.

(a) Image segmentation

Raw image

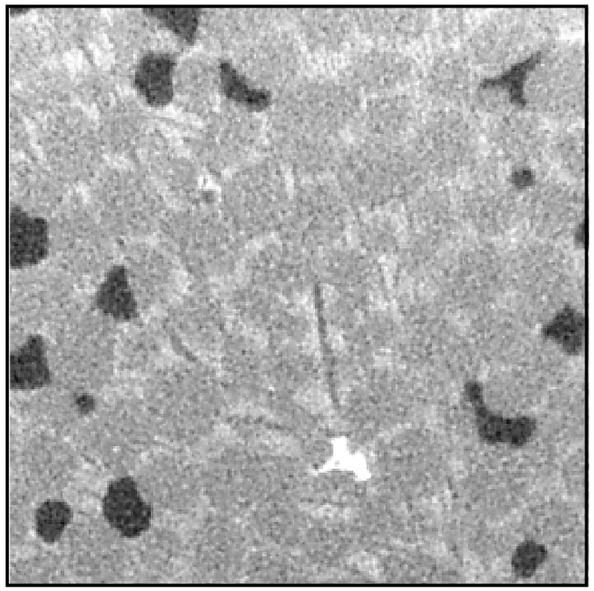

Isolated crystals

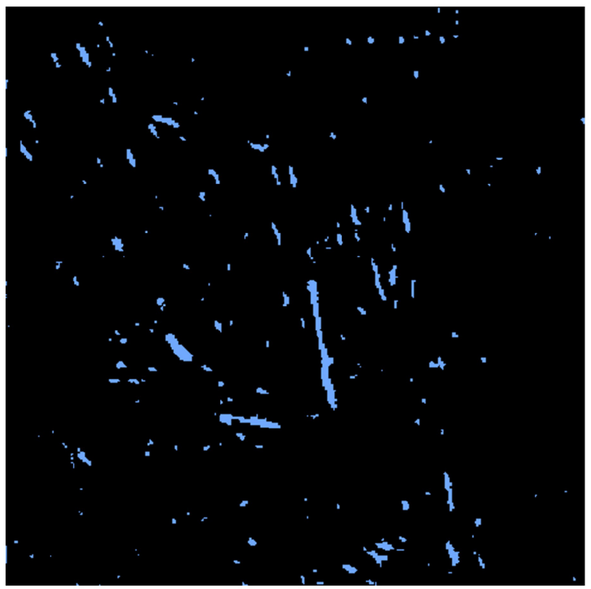

(b) Orientation extraction

Crystal demo

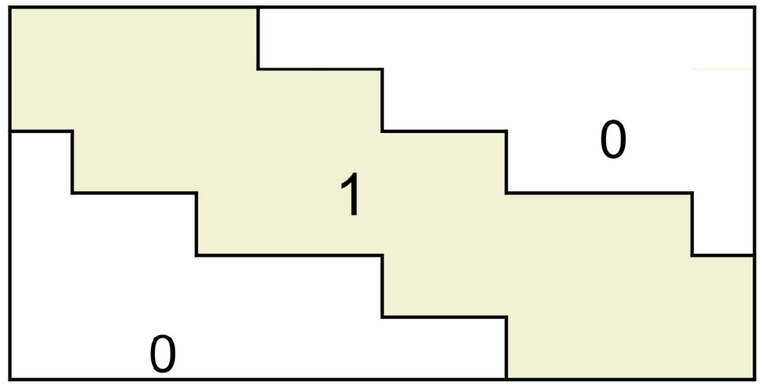

Crystal voxel values= 1

PCA of crystals

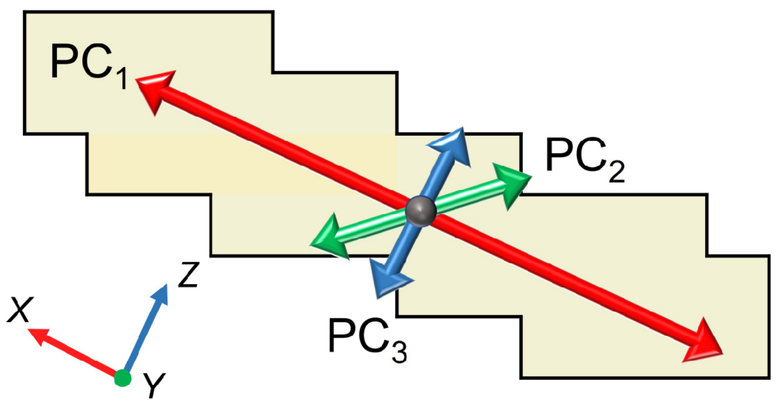

PC_3: (0.022, -0.999, -0.019)

(c) Color assignment

Voxel assignment

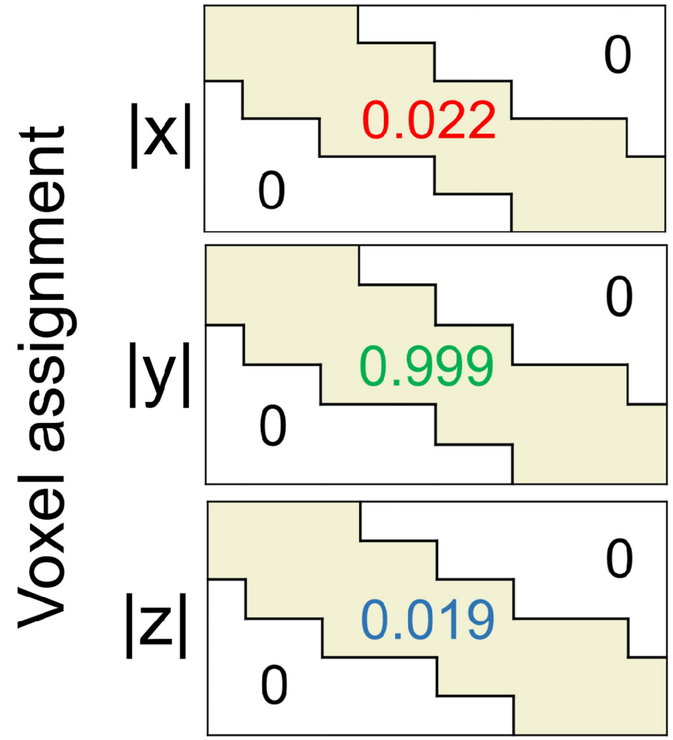

RGB visualization

X = 0.022	× 255 =	006	R
Y = 0.999		255	G
Z = 0.019		005	B

(006, 255, 005)

Figure 5.

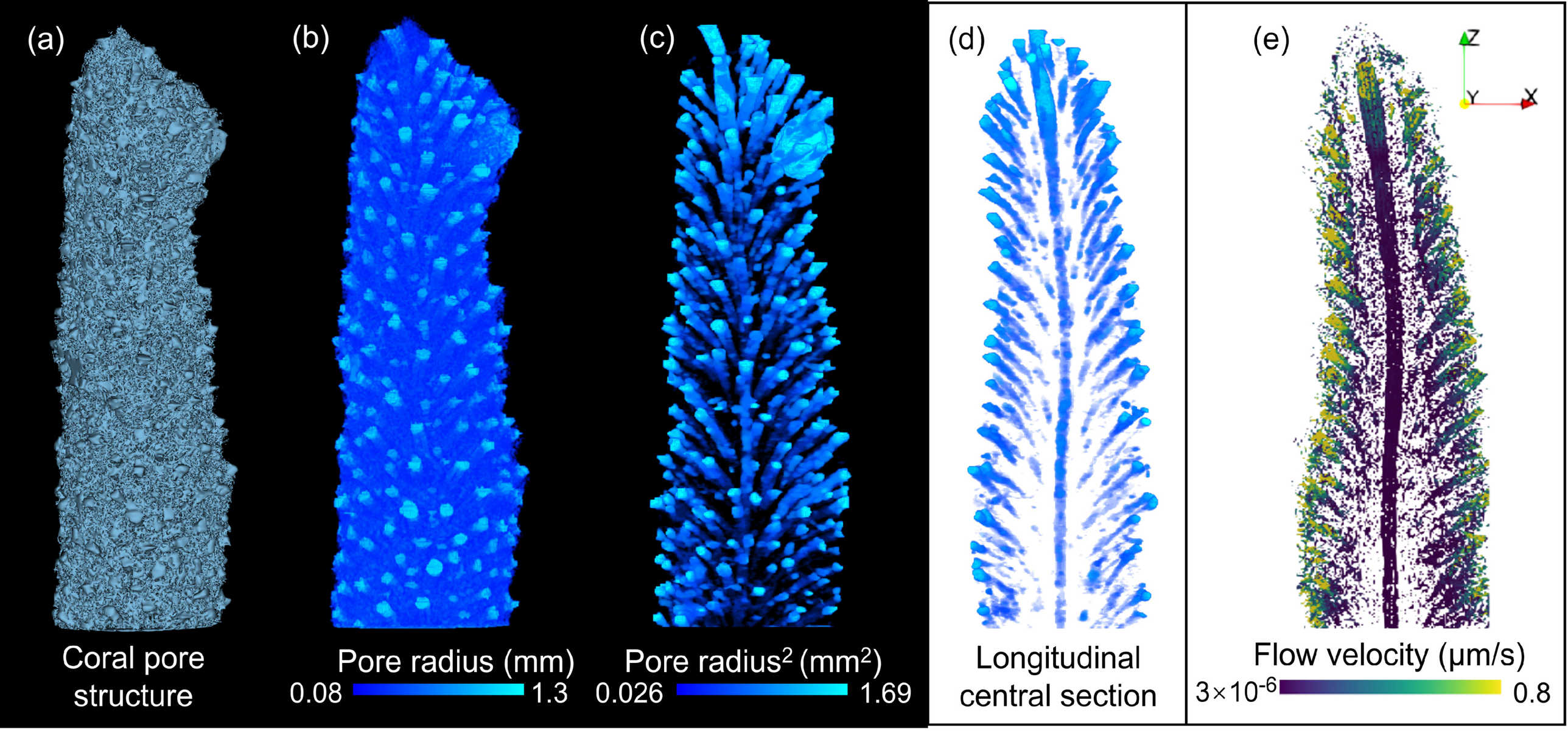
(a)
(b)
(c)
(d)
(e)
Z
Y
X
Coral pore structure
Pore radius (mm)
0.08
1.3
Pore radius² (mm²)
0.026
1.69
Longitudinal central section
Flow velocity (μm/s)
3×10-6
0.8

Figure 6.

(a)

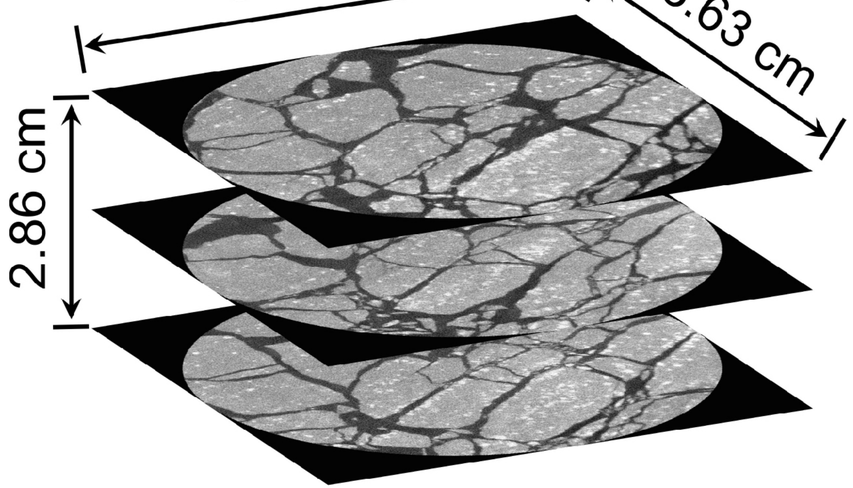
3.63 cm
3.63 cm
2.86 cm

(b)

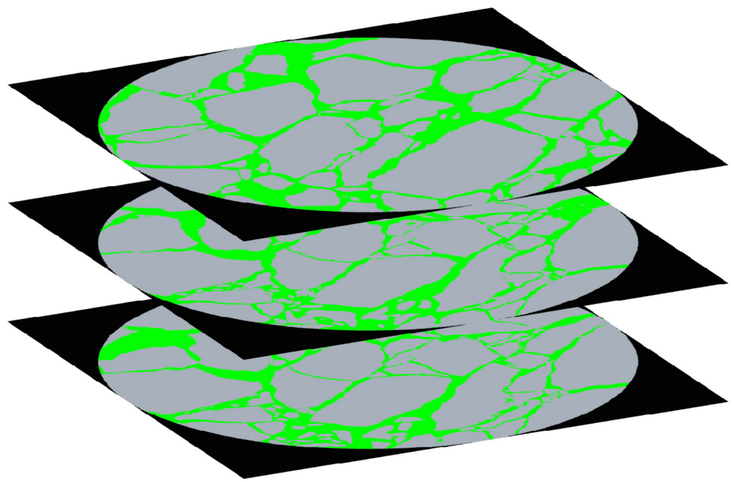

(c)

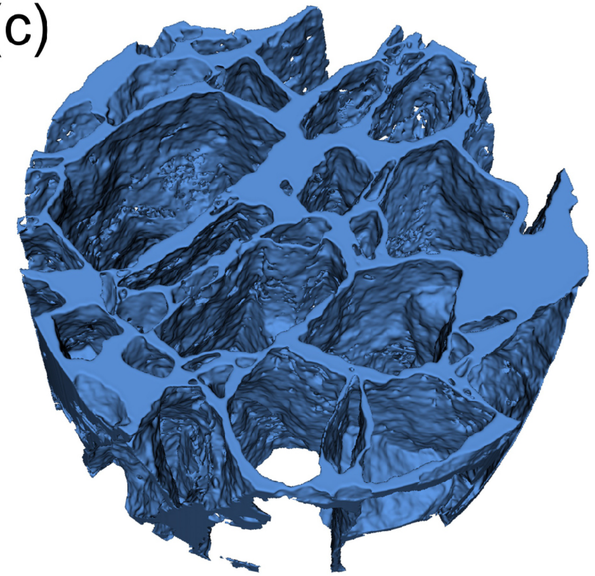

(d)

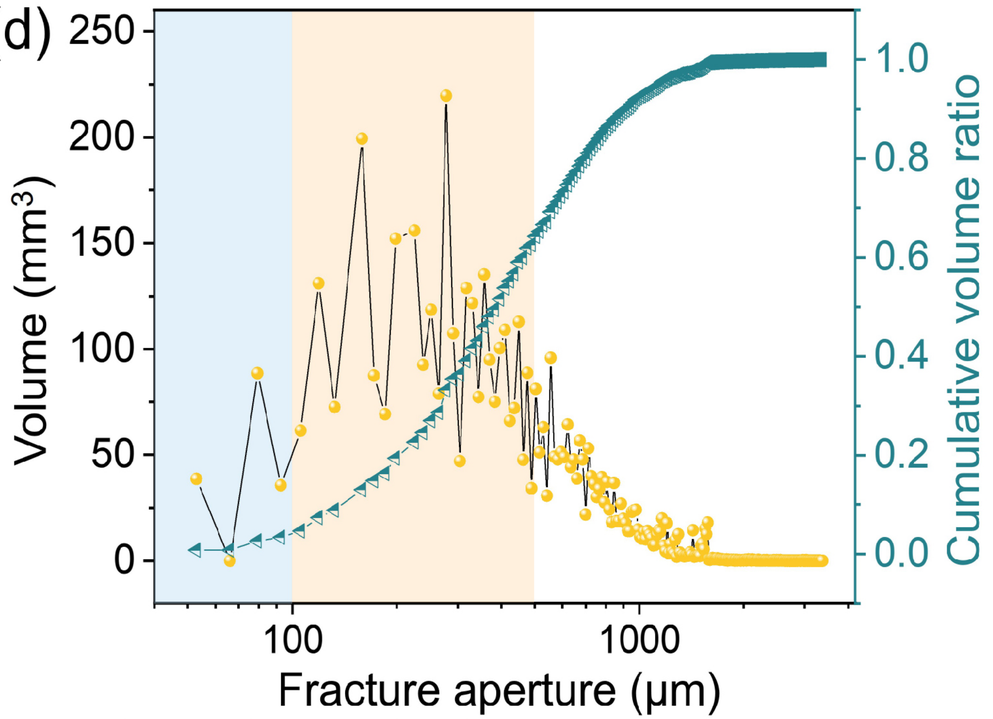
250
200
150
100
50
0
Volume (mm3)
1.0
0.8
0.6
0.4
0.2
0.0
Cumulative volume ratio
100
1000
Fracture aperture (μm)

(e)

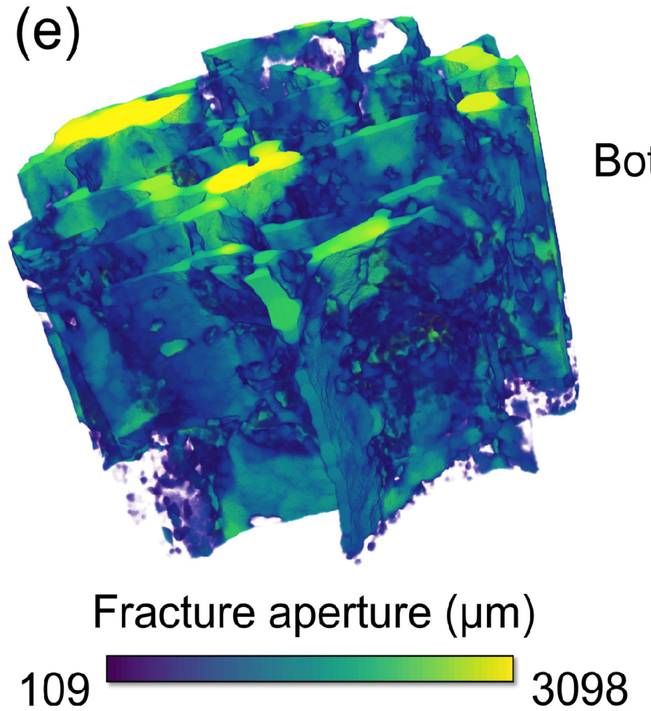
Fracture aperture (μm)
109
3098

(f)

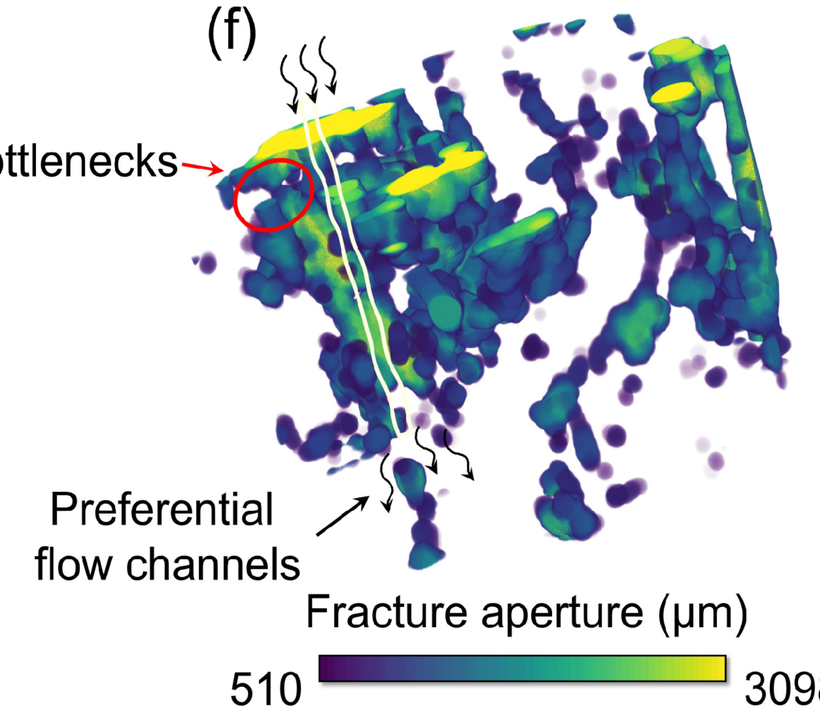
Bottlenecks
Preferential
flow channels
Fracture aperture (μm)
510
3098

Figure 7.

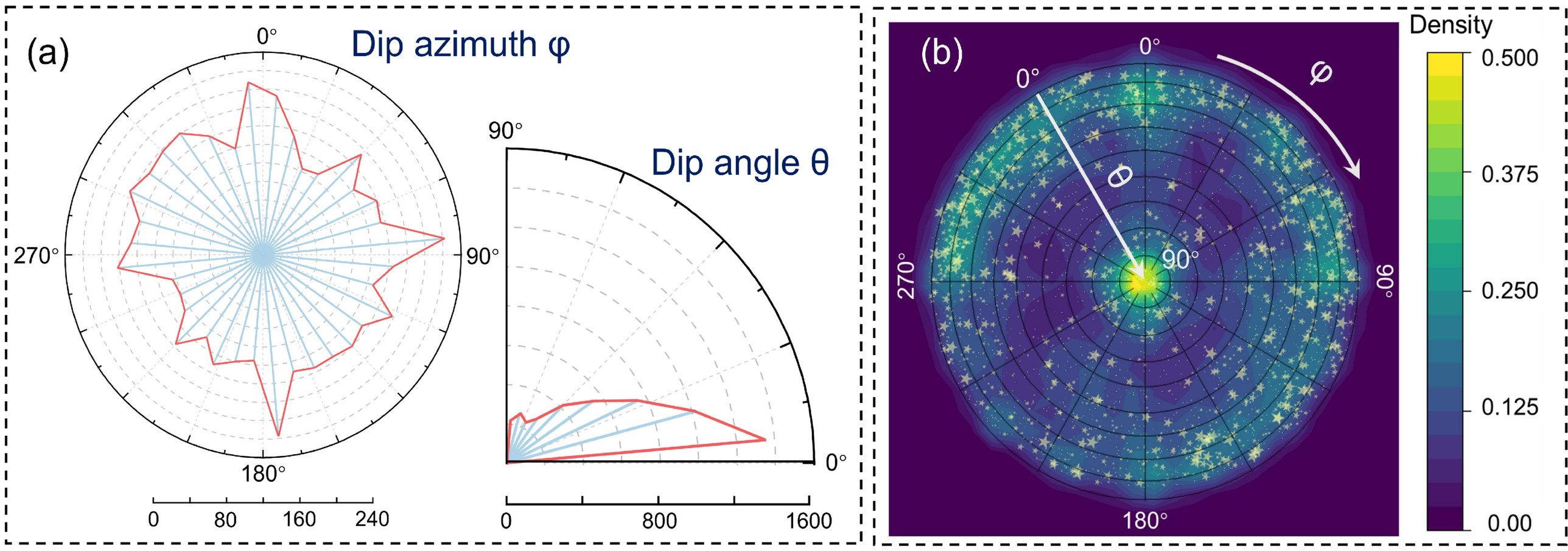
(a)
Dip azimuth φ
0°
90°
180°
270°
0
80
160
240
Dip angle θ
90°
0°
0
800
1600
(b)
0°
0°
φ
θ
90°
270°
90°
180°
Density
0.500
0.375
0.250
0.125
0.00

Figure 8.

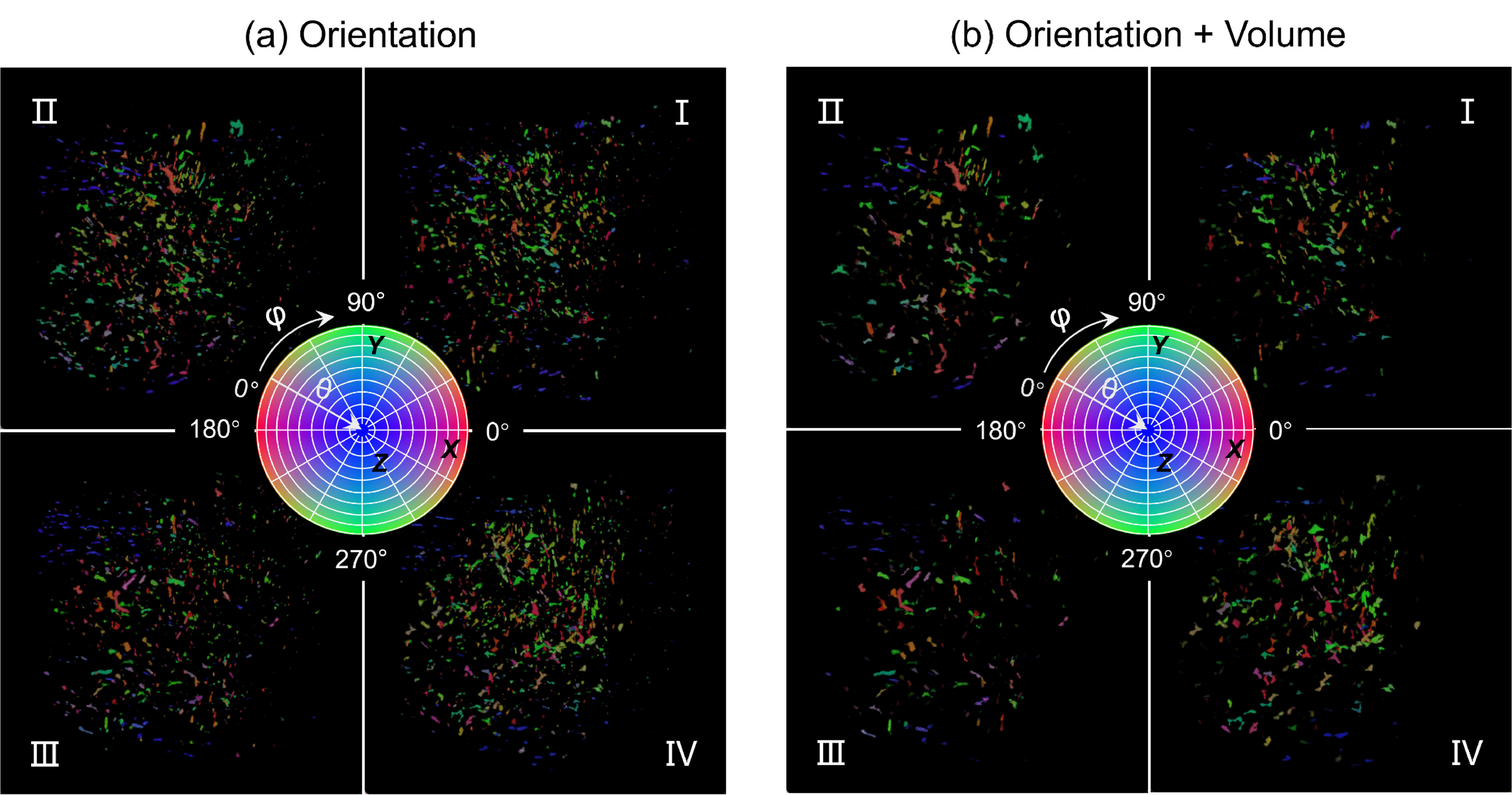
(a) Orientation
(b) Orientation + Volume
Ⅱ
Ⅰ
Ⅲ
Ⅳ
φ
90°
0°
180°
0°
270°
θ
Y
X
Z

Figure 9.

Original model

Simplified model

(a) (b) (c) (d) (e) (f)

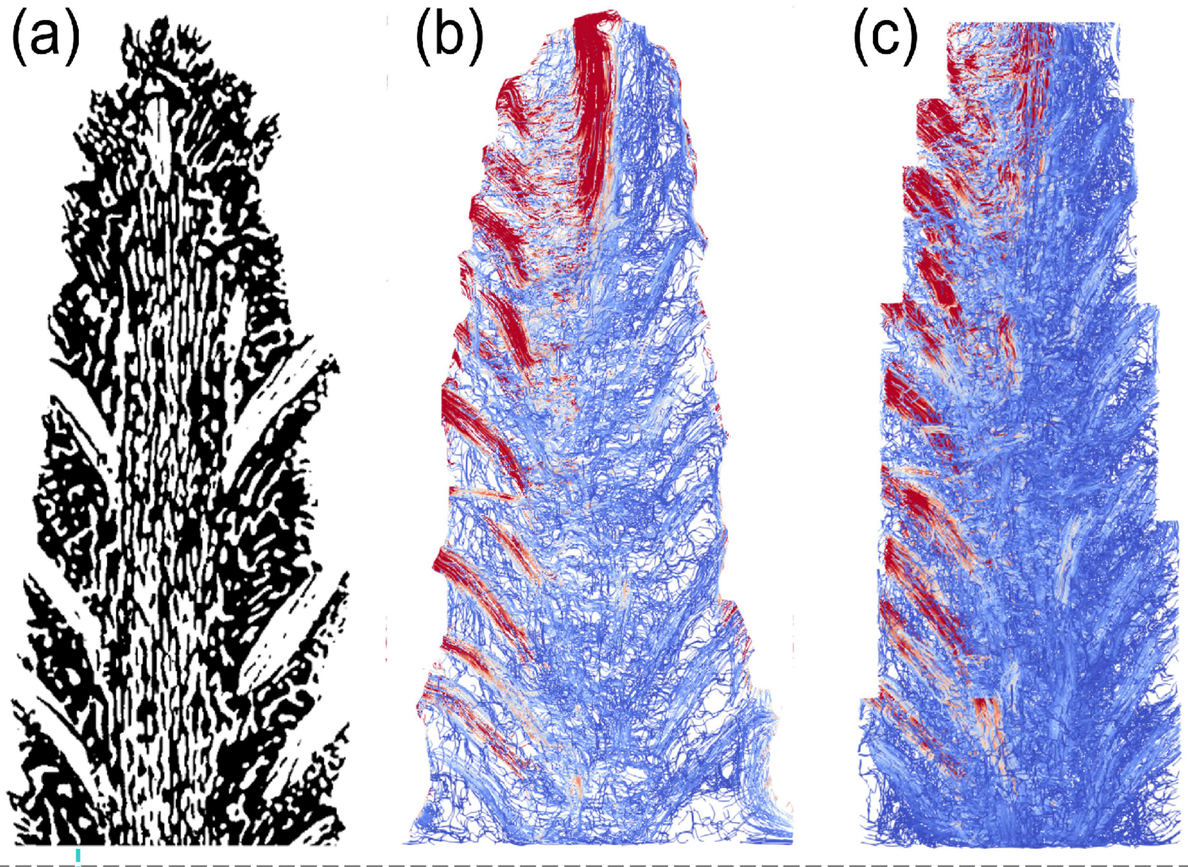

2×10^{-6} Flow velocity (μm/s) 0.66

(g) Model simplification workflow

Main branchlets » Central dilation » Overall connectivity

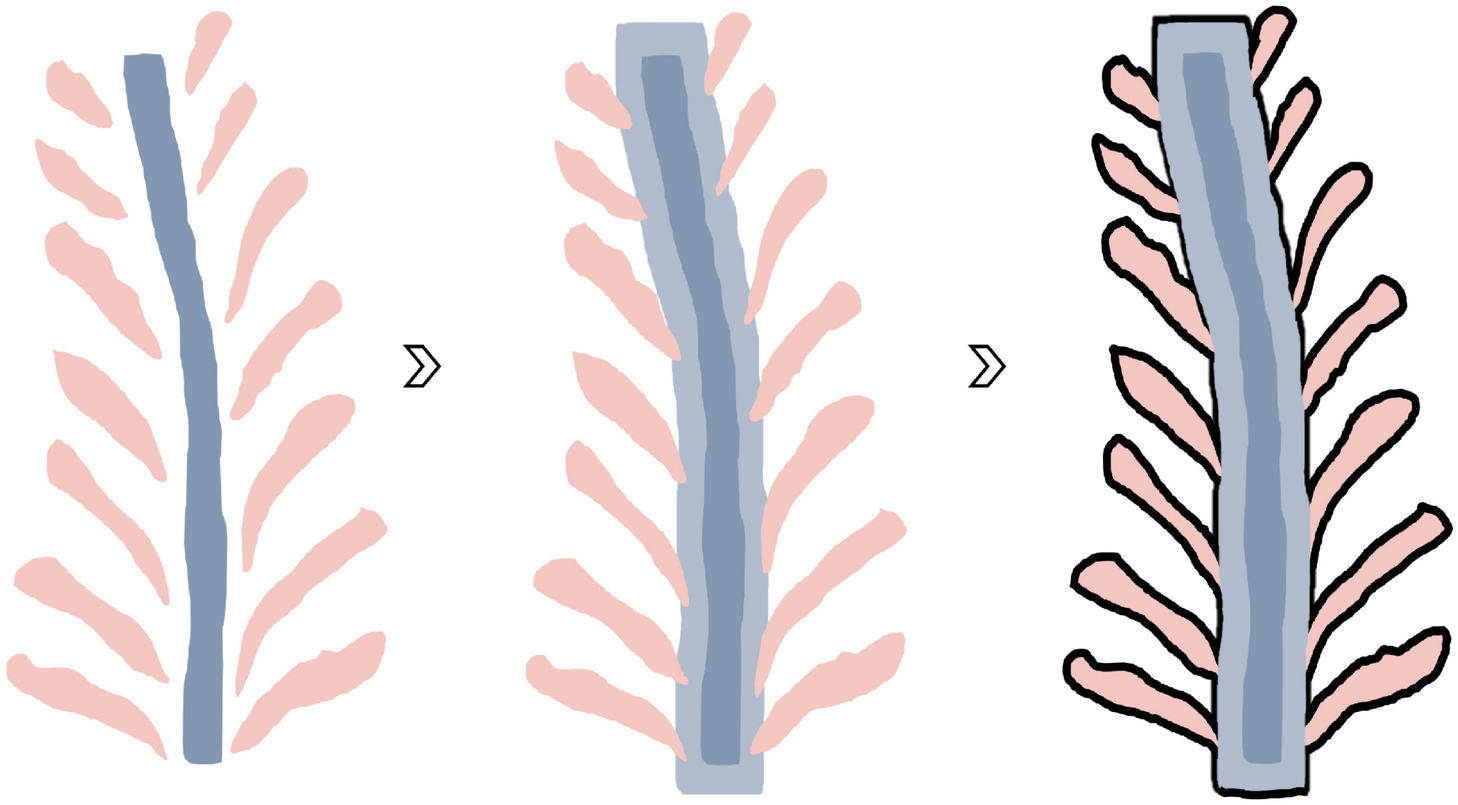

Branchlets Central canal Dilated canal Identified region

(h) Velocity comparison

Selected regions

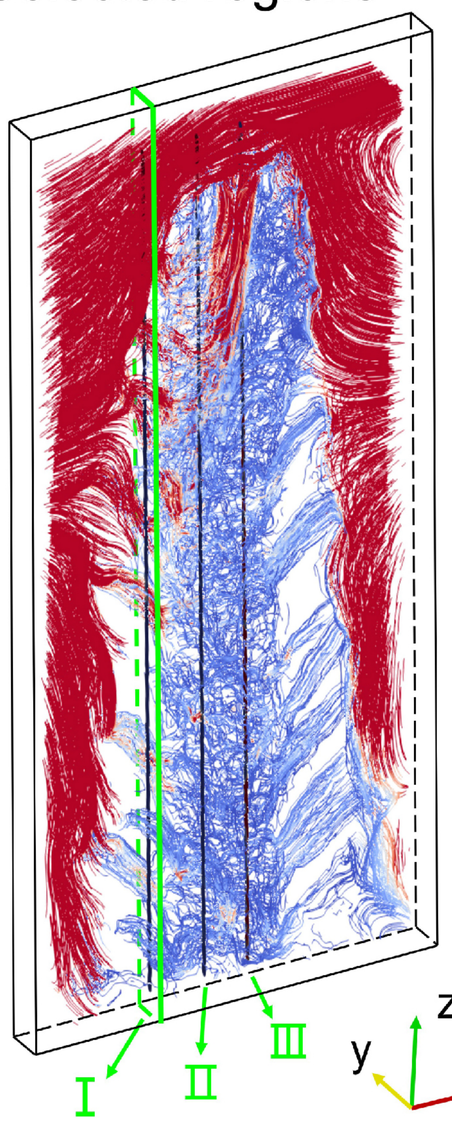

Flow velocity (μm/s)

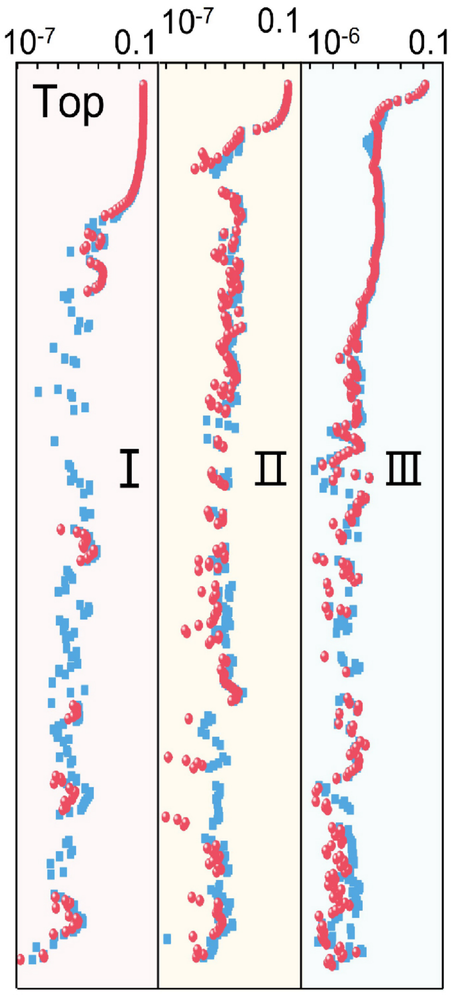

Figure 10.

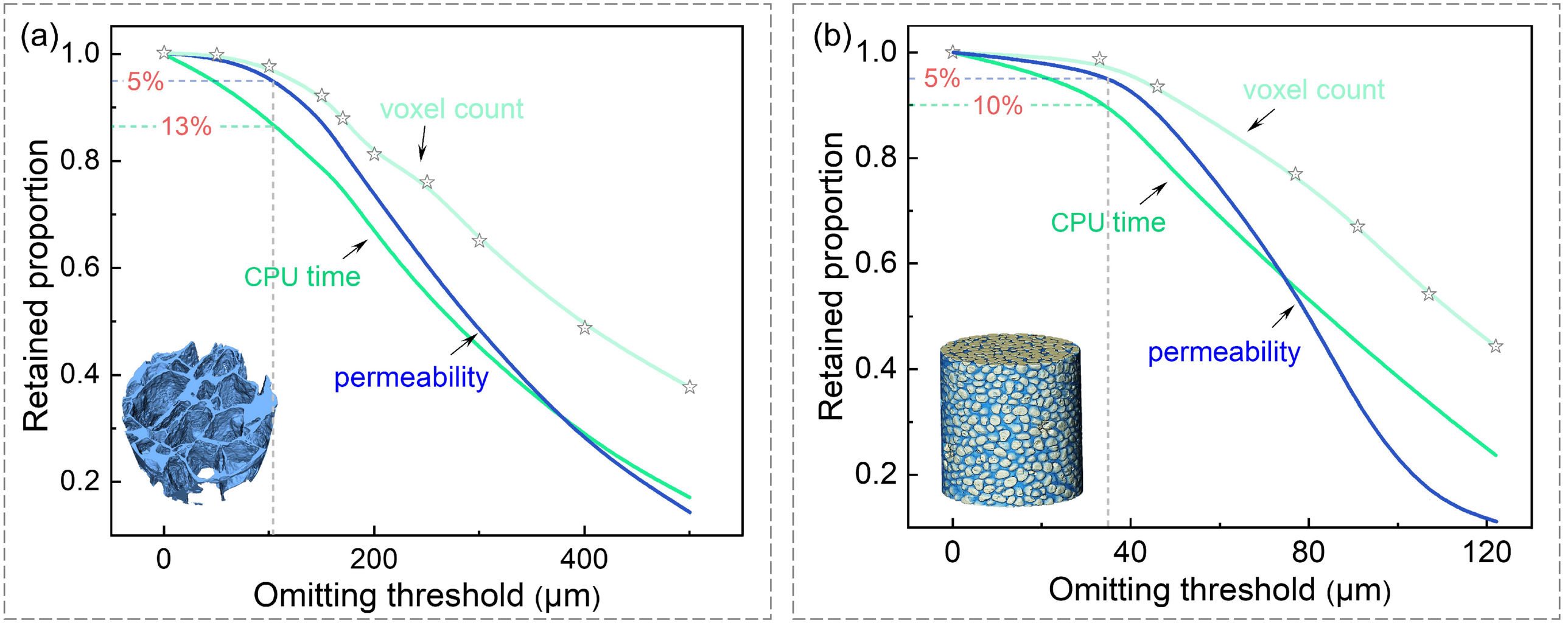
(a)
1.0
0.8
0.6
0.4
0.2
Retained proportion
5%
13%
voxel count
CPU time
permeability
0
200
400
Omitting threshold (μm)
(b)
1.0
0.8
0.6
0.4
0.2
Retained proportion
5%
10%
voxel count
CPU time
permeability
0
40
80
120
Omitting threshold (μm)